

## **Publications:**

### **Paper 1:**

**Implementation of a Reduced Field-of-View Method for Dynamic MR Imaging Using Navigator Echoes.**

### **Authors:**

**Walid E Kyriakos, Lawrence P. Panych, Gary P. Zientara, Ferenc A. Jolesz.**

### **Journal:**

**Journal of Magnetic Resonance Imaging (JMRI)  
1997, 7:376-381.**



# Implementation of a Reduced Field-of-View Method for Dynamic MR Imaging Using Navigator Echoes

Walid E. Kyriakos, MS • Lawrence P. Panych, PhD • Gary P. Zientara, PhD • Ferenc A. Jolesz, PhD

A new technique was designed and implemented that increases imaging speed in dynamic imaging in which change is restricted to a fraction of the full field of view (FOV). The technique is an enhancement of a reduced FOV method first reported by Hu and Parrish. This enhancement extends the use of the Hu and Parrish method to cases in which there is cyclic motion throughout the entire FOV that normally would be aliased into the reduced FOV. This method requires the initial acquisition of a number of baseline k-space data sets to characterize the background physiological motion during imaging. Projection navigator echoes along both the phase- and the frequency-encoded directions are acquired and used to correct for motion outside the reduced FOV. Automatic placement or repositioning of the updated fraction of the FOV using navigators also is investigated. With this method, when using a 32-echo rapid acquisition with relaxation enhancement (RARE) sequence, single-shot updates of T2-weighted, 128 × 128 pixel images are obtained, yielding a fourfold increase in temporal resolution compared to full k-space update methods.

**Index terms:** k-space sampling • Image aliasing • Projection navigator echoes • Reduced FOV

JMRI 1997; 7:376-381

**Abbreviations:** FOV = field of view, GRASE = gradient and spin echo, RARE = rapid acquisition with relaxation enhancement, rFOV = reduced field of view, ROPE = respiratory-ordered phase encoding, SNR = signal-to-noise ratio.

From the Department of Electrical Engineering, Boston University, Boston, MA 02215 (W.E.K.); and the Department of Radiology, Harvard Medical School and Brigham and Women's Hospital, 75 Francis Street, Boston, MA 02115 (L.P.P., G.P.Z., F.A.J.). Received April 15, 1996; revision requested July 24; revision received October 4; accepted October 7. Supported by a Whitaker Foundation Biomedical Engineering Research grant (to L.P.P.), National Institutes of Health Grants No. CA45743-06 and No. P01CA67165-01. Address reprint requests to L.P.P.

© ISMRM, 1997

IN SOME APPLICATIONS of dynamic MRI, change is well localized to a small fraction of the field of view (FOV). This occurs frequently in interventional MRI (1-3), during monitoring of the insertion of a catheter or biopsy needle, or during the application of therapy (4). In these cases, there is a great deal of redundancy of data acquisition if the entire FOV is continually updated; therefore, several methods that attempt to focus only on the region of the change have been developed. In previous work with wavelet encoding, for example, Panych et al (5) investigated methods to zoom in only on those parts of the FOV in which change occurs. Because much fewer data are needed if only a part of the FOV is updated, these reduced FOV (rFOV) approaches have the potential to greatly increase temporal resolution.

Recently, Hu and Parrish (6) presented a Fourier-encoding method designed to enhance imaging speed within an rFOV. Their method is based on the undersampling of k space to rapidly acquire the dynamic image updates yielding a considerable improvement in time resolution. However, the performance of this method is constrained strongly by the satisfaction of two strict assumptions. The first of these assumptions is that the change in the dynamic image is restricted physically to a predetermined rFOV, because any change occurring outside of this area is aliased into it after reconstruction, resulting in a serious deterioration of the image. The second assumption is that the position of the rFOV in which change is supposed to occur is known a priori to allow for the correct placement within the full FOV during the dynamic reconstruction.

Practically the first assumption cannot be satisfied when there is physiological motion occurring in the entire FOV, for example, during abdominal imaging. In brain imaging, although motion generally is less problematic, there is often slight bulk head motion, violating the assumption of localized change among a static background. The second assumption that the rFOV position is known could be satisfied realistically in interventional MRI applications, in which the operator knows a priori the location of the introduced change. The success of the method, however, would depend in this case on the correct estimation of the relative position of the change within the entire FOV, and this may be subject to error.

We present herein a technique designed to deal with the first limitation of the original rFOV approach and extend its use to cases in which cyclic motion may occur throughout the entire FOV. In our method, data from a

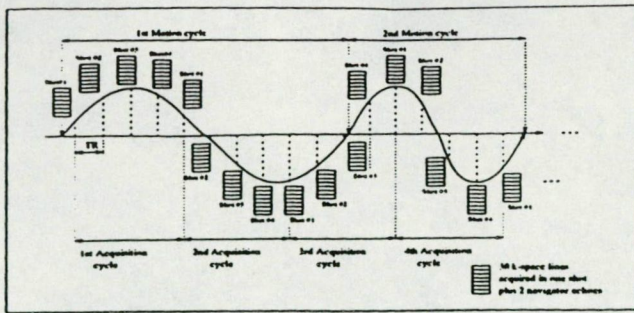


**Figure 2.** Schematic representation of the correspondence of baseline data acquisition to physiological motion cycle. Data are acquired in this fashion over several cycles of the physiological motion. Then, data from all cycles are organized into four groups, depending on their shot number.

serve to locate its time point within the physiological motion cycle. Let  $N_y(x)$  designate the projection navigator along the frequency-encoded direction  $x$ , where  $i$  is the associated shot number ( $i = 1..4$ ) and  $j$  is an index representing this order of acquisition in the baseline acquisition series and, most likely, distinguishing a different time point in the motion cycle. Let  $N_y(y)$  designate the projection navigator along the phase-encoded direction  $y$ . Once the baseline data sets have been acquired and stored in the above fashion, the dynamic process is initiated.

**Dynamic choice of the baseline data.**—Consider now the data acquisition as change is occurring. With each 32-echo shot during dynamic imaging, we acquire a set of 30 k-space lines plus two projection navigator echoes. Let  $D_i(x)$  designate the dynamic navigator echo along the frequency-encoded direction  $x$  and let  $D_i(y)$  designate the dynamic navigator echo along the phase-encoded direction  $y$ , with  $i$  being the shot number. The k-space lines acquired by the  $i$ th shot number are indicated by Equation [1].

Every pair of dynamic navigators  $D_i(x)$  and  $D_i(y)$  is compared to each of the baseline navigator pairs  $N_y(x)$  and  $N_y(y)$  from all four baseline data groups to get the best baseline fit minimizing the mean squared error of the difference between navigator projections:

$$r_y = \int |D_i(x) - N_y(x)|^2 dx + \int |D_i(y) - N_y(y)|^2 dy \quad (2)$$

For every shot,  $i$  ( $i = 1..4$ ), we select from the baseline information,  $N_y(x)$  and  $N_y(y)$ , that minimizes  $r_y$ , yielding four subsets ( $i = 1..4$ ) of k-space data corresponding to the best baseline image match according to the mean squared error criterion. For example, for shot  $i = 1$ , the  $j = 7$ th navigator might minimize Equation [2], whereas for shot  $i = 2$ , the  $j = 16$ th navigator might be optimal. The selected four subsets ( $i = 1..4$ ) represent a complete baseline image data set. The k-space data sampled from the current shot provide the dynamic update data. Reconstruction of the dynamic update now can be performed similarly to the Hu and Parrish method outlined previously.

It is useful to note here that the ordering of k-space acquisition in our method is fixed throughout the experiment and does not depend on the state of the physiological cycle, unlike the respiratory-ordered phase encoding (ROPE) (10) method, which uses previous knowledge of the distribution function of an external breathing signal to dynamically order the acquisition of individual k-space lines. Instead, we use navigator echo information to pick,

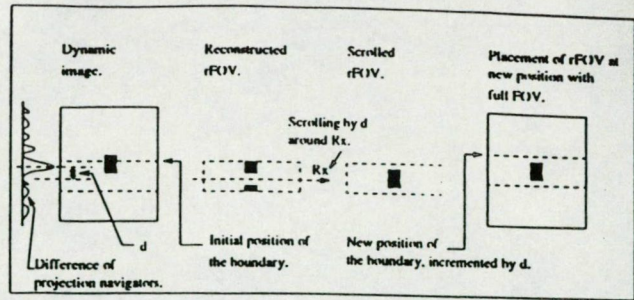


**Figure 3.** Scheme for placement of the rFOV within the baseline image to avoid wraparound when change crosses the boundary of a rFOV. (Computations progress as shown from left to right.) First, the reconstructed rFOV data are scrolled by a certain amount ( $d$ ) equal to the distance between the peak of the difference navigator and the midline of the rFOV to place the peak of the change in the center of the rFOV. The rFOV is then placed in the baseline image after adjusting its position by the same amount as the scrolling.

off-line, the best baseline data set to use when reconstructing the dynamic data.

**Placement of rFOV.**—The task of placing the rFOV within the chosen baseline image remains after the difference image is computed and the rFOV is reconstructed. In our method, because we chose the rFOV to be one quarter of the FOV, we need to pick one of four possible quarter segments in the phase-encoding direction into which to add the difference image. If the change crosses the boundary of an rFOV, the reconstruction of the difference of the dynamic subset would yield a  $32 \times 128$  image in which the change is separated into two parts at the edges due to aliasing (wraparound).

A postprocessing computation is used to properly place the rFOV in the FOV and to avoid wraparound. The location in the phase-encoding direction of the change must be estimated either by direct manual prescription or by an automated approach. We investigated an automated method of placement using information from the projection navigators in the phase-encoding direction. In the automatic method, the difference between the projection navigator in the phase-encoding direction of the dynamic update and the average of the navigators in the phase-encoding direction of the chosen baseline image is computed, and the peak at which the maximum of this difference occurs is located. After the peak of the change is determined either by the manual or automatic method, the rFOV is then scrolled in the spatial domain as shown in Figure 3, to place the peak of the change in the middle of the rFOV. The altered rFOV is then placed in the chosen baseline image offset from its original position as shown in Figure 3.

The complex-valued difference image is added to the chosen complex-valued baseline image to get a dynamic update. However, in the case in which the change has high contrast, and for the purpose of reducing the aliasing within the rFOV, the difference image can be weighted by a reduction factor between 0 and 1, before adding the rFOV to the baseline image. This weighting is a compromise between properly updating the image and reducing the aliasing from change occurring outside the rFOV.

## • RESULTS

All experiments were performed on a 1.5-T SIGMA (General Electric Medical Systems, Milwaukee, WI) clinical MRI system. We performed two sets of experiments to

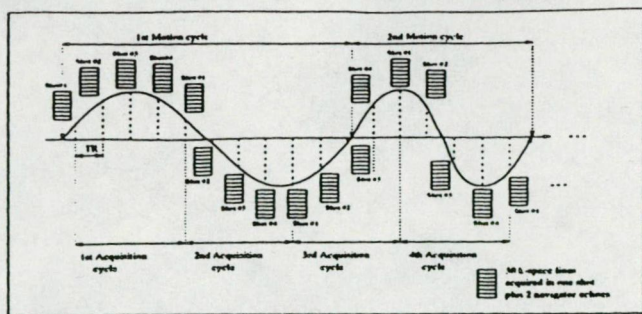


**Figure 2.** Schematic representation of the correspondence of baseline data acquisition to physiological motion cycle. Data are acquired in this fashion over several cycles of the physiological motion. Then, data from all cycles are organized into four groups, depending on their shot number.

serve to locate its time point within the physiological motion cycle. Let  $N_y(x)$  designate the projection navigator along the frequency-encoded direction  $x$ , where  $i$  is the associated shot number ( $i = 1..4$ ) and  $j$  is an index representing this order of acquisition in the baseline acquisition series and, most likely, distinguishing a different time point in the motion cycle. Let  $N_y(y)$  designate the projection navigator along the phase-encoded direction  $y$ . Once the baseline data sets have been acquired and stored in the above fashion, the dynamic process is initiated.

**Dynamic choice of the baseline data.**—Consider now the data acquisition as change is occurring. With each 32-echo shot during dynamic imaging, we acquire a set of 30 k-space lines plus two projection navigator echoes. Let  $D_i(x)$  designate the dynamic navigator echo along the frequency-encoded direction  $x$  and let  $D_i(y)$  designate the dynamic navigator echo along the phase-encoded direction  $y$ , with  $i$  being the shot number. The k-space lines acquired by the  $i$ th shot number are indicated by Equation [1].

Every pair of dynamic navigators  $D_i(x)$  and  $D_i(y)$  is compared to each of the baseline navigator pairs  $N_y(x)$  and  $N_y(y)$  from all four baseline data groups to get the best baseline fit minimizing the mean squared error of the difference between navigator projections:

$$r_y = \int |D_i(x) - N_y(x)|^2 dx + \int |D_i(y) - N_y(y)|^2 dy \quad (2)$$

For every shot,  $i$  ( $i = 1..4$ ), we select from the baseline information,  $N_y(x)$  and  $N_y(y)$ , that minimizes  $r_y$ , yielding four subsets ( $i = 1..4$ ) of k-space data corresponding to the best baseline image match according to the mean squared error criterion. For example, for shot  $i = 1$ , the  $j = 7$ th navigator might minimize Equation [2], whereas for shot  $i = 2$ , the  $j = 16$ th navigator might be optimal. The selected four subsets ( $i = 1..4$ ) represent a complete baseline image data set. The k-space data sampled from the current shot provide the dynamic update data. Reconstruction of the dynamic update now can be performed similarly to the Hu and Parrish method outlined previously.

It is useful to note here that the ordering of k-space acquisition in our method is fixed throughout the experiment and does not depend on the state of the physiological cycle, unlike the respiratory-ordered phase encoding (ROPE) (10) method, which uses previous knowledge of the distribution function of an external breathing signal to dynamically order the acquisition of individual k-space lines. Instead, we use navigator echo information to pick,

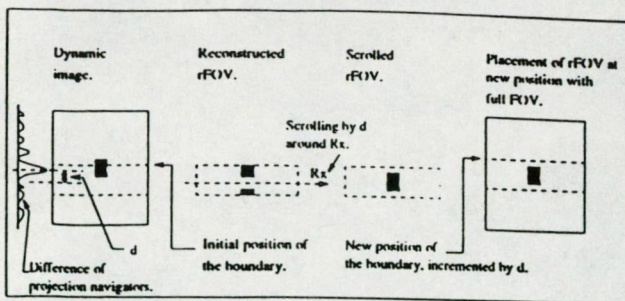


**Figure 3.** Scheme for placement of the rFOV within the baseline image to avoid wraparound when change crosses the boundary of a rFOV. (Computations progress as shown from left to right.) First, the reconstructed rFOV data are scrolled by a certain amount ( $d$ ) equal to the distance between the peak of the difference navigator and the midline of the rFOV to place the peak of the change in the center of the rFOV. The rFOV is then placed in the baseline image after adjusting its position by the same amount as the scrolling.

off-line, the best baseline data set to use when reconstructing the dynamic data.

**Placement of rFOV.**—The task of placing the rFOV within the chosen baseline image remains after the difference image is computed and the rFOV is reconstructed. In our method, because we chose the rFOV to be one quarter of the FOV, we need to pick one of four possible quarter segments in the phase-encoding direction into which to add the difference image. If the change crosses the boundary of an rFOV, the reconstruction of the difference of the dynamic subset would yield a  $32 \times 128$  image in which the change is separated into two parts at the edges due to aliasing (wraparound).

A postprocessing computation is used to properly place the rFOV in the FOV and to avoid wraparound. The location in the phase-encoding direction of the change must be estimated either by direct manual prescription or by an automated approach. We investigated an automated method of placement using information from the projection navigators in the phase-encoding direction. In the automatic method, the difference between the projection navigator in the phase-encoding direction of the dynamic update and the average of the navigators in the phase-encoding direction of the chosen baseline image is computed, and the peak at which the maximum of this difference occurs is located. After the peak of the change is determined either by the manual or automatic method, the rFOV is then scrolled in the spatial domain as shown in Figure 3, to place the peak of the change in the middle of the rFOV. The altered rFOV is then placed in the chosen baseline image offset from its original position as shown in Figure 3.

The complex-valued difference image is added to the chosen complex-valued baseline image to get a dynamic update. However, in the case in which the change has high contrast, and for the purpose of reducing the aliasing within the rFOV, the difference image can be weighted by a reduction factor between 0 and 1, before adding the rFOV to the baseline image. This weighting is a compromise between properly updating the image and reducing the aliasing from change occurring outside the rFOV.

## • RESULTS

All experiments were performed on a 1.5-T SIGNA (General Electric Medical Systems, Milwaukee, WI) clinical MRI system. We performed two sets of experiments to



**Figure 4.** Results of abdominal imaging during breathing. The block of 20 images on the left shows the dynamic updates obtained during dynamic acquisition using the reduced FOV method with navigators. The strip of live images on the right shows the slow updates available using a full set of acquired phase encodes. For every four dynamic updates, one full slow update is acquired. The time sequence is from left to right and from top to bottom.

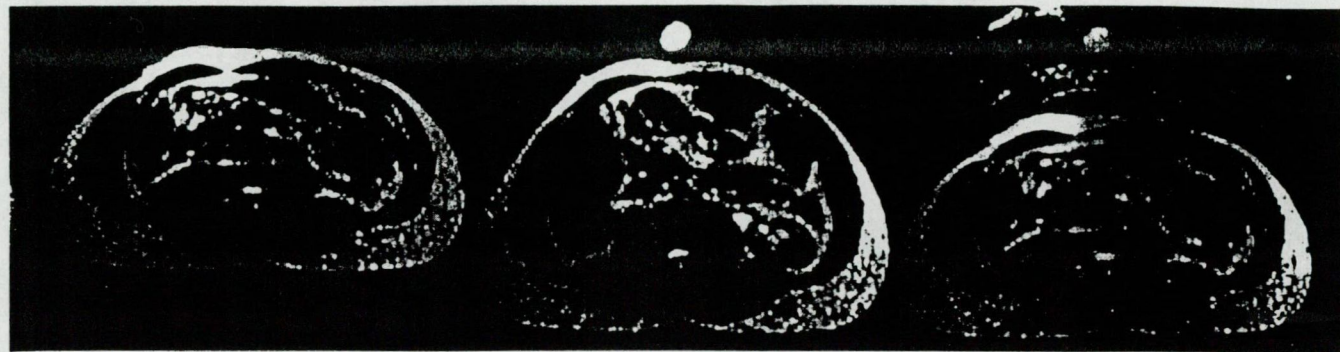


**Figure 5.** Result of the application of the Hu and Parrish technique to a case in which physiological motion occurs. The image on the left shows an abdomen before inhaling. The image in the center shows the same abdomen after introducing a water sample (appears as bright circle). The image on the right shows the result of applying the Hu and Parrish approach. Excessive motion artifact can be seen within the rFOV.

test the performance of our method. In both of our experiments, image resolution was  $128 \times 128$  pixels. We used a 32-echo RARE sequence, TR = 2 seconds, TE = 10 msec, 320 msec per shot, obtaining one dynamic image update with a single shot.

In the first experiment, we acquired one abdominal slice during respiratory motion while moving a gadolinium-doped water sample across the abdomen. We collected eight baseline data sets before introducing the water sample, thus acquiring 32 consecutive shots during normal breathing. At the end of baseline acquisition, the data were organized into four groups as described previously. Next, a water sample was rolled above and across the abdomen of the volunteer, and dynamic acquisition was initiated. In this case, we had knowledge of the position of the rFOV within the baseline image (surface of the abdomen) for placement of the difference im-

Figure 4 shows the series of dynamic images obtained using this method. The slow update, obtained after every four dynamic updates, is shown on the right side of Figure 4. In this series, we can see the position of the water sample changing, as well as the background profile of the abdomen due to respiratory motion. Some artifact can be detected in the dynamic series. This artifact depends on the density of the coverage of the motion cycle represented in the baseline imaging and is independent of the speed of the motion, as long as no considerable motion occurs within the 320-msec time that it would take to acquire one shot. Figure 5 shows the result of applying the original method without navigators. The substantial presence of artifact within the rFOV makes it difficult to discern any structural detail or the position of the change.

A second set of experiments was performed to test the automatic placement scheme. A water sample was moved across a spherical water phantom, and the automatic

placement approach described in the preceding section was used. The left side of Figure 6 shows results obtained in this case. The dynamic update reconstructed using the automatic placement approach can be seen at the top left of Figure 6. Below the image is the plot of the difference between the dynamic navigator and the chosen baseline average navigator. This plot shows a dominant peak, allowing for the unambiguous placement of the dynamic rFOV within the baseline image.

We tried to follow the movement of the same water sample along a human head using this automatic placement method. The resulting dynamic image series was characterized by discontinuous jumps of the sample and erroneous placement inside the FOV. We then reconstructed the dynamic images using prior knowledge of the position of the rFOV and plotted the difference navigator for comparison. A sample of the results of this experiment at one time point is shown on the right side of Figure 6. An examination of the plot of the difference between the dynamic navigator and the chosen baseline average navigator, shown at the bottom right side of Figure 6, demonstrates the inability of the difference navigator to unambiguously locate the change. This can be attributed to the fact that slight difference in position between highly contrasted components (relative to contrast of change versus background) of the baseline image and the dynamic image (full FOV) are greater in magnitude than the difference signal coming from the water sample position.

#### • DISCUSSION

We have designed a method to address the major limitation of the rFOV technique as it was originally described by Hu and Parrish (6), especially in the cases in which significant physiological motion occurs during the dynamic imaging process. By incorporating the use of navigator echoes, our principal goal was to reduce motion

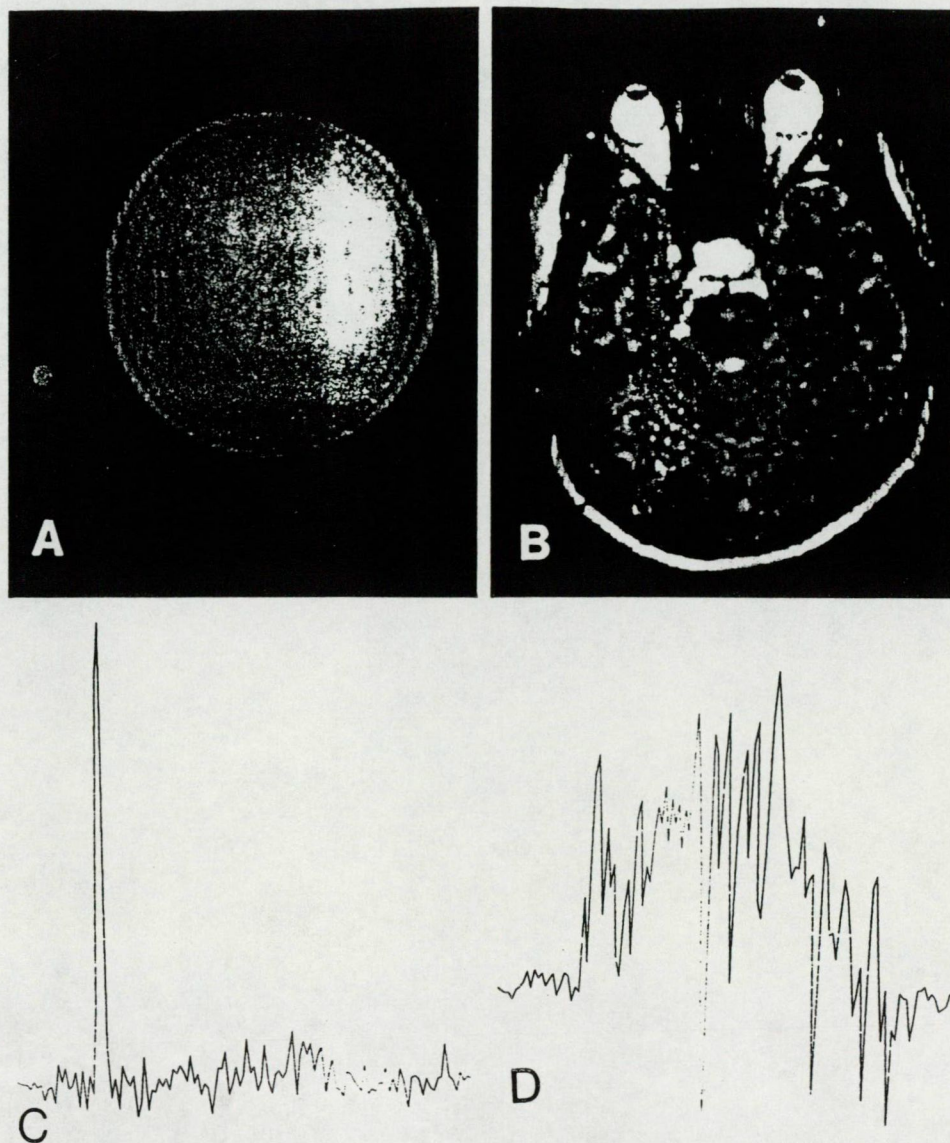


**Figure 6.** Automatic placement using the projection navigator echo along the phase-encoded direction (horizontal direction in this example). On the left, the case of phantom imaging is shown and the position of the peak in the difference of projections clearly determines the position of the change within the FOV. At right is an image of a brain imaging case in which the difference navigator does not unambiguously determine the position of the change.

artifacts within the rFOV by use of baseline data that closely represent the physiological motion that occurs outside the rFOV but within the full FOV. Secondly, we tested a simple approach using projection navigators to automatically place the rFOV within the full FOV.

Significant reduction of motion artifacts within the rFOV was achieved over the initial method with the use of navigators. In the abdominal imaging experiments, for example, we were able to follow the dynamic change regardless of the background physiological motion. Furthermore, because our updates are acquired in a single shot, the remaining motion artifacts are TR independent. T2-weighted spin-echo snapshot updates of an abdominal slice during breathing ( $128 \times 128$  image matrix) were obtained despite significant motion occurring within the TR period.

The projection navigator method was not successful when applied to the task of automatic placement of the rFOV. The automatic placement algorithm was based on the difference between the dynamic and the baseline projection navigator echoes along the phase-encoding direc-

tion. This particular method is apparently too sensitive to even small amounts of motion to be useful in the general case. We are presently investigating a more sophisticated adaptive approach of rFOV placement that is based on locating the bulk position of the change using low-frequency information and then following a multi-resolution search strategy to zoom in on the position of the change.

In the implementation presented herein, two echoes in the 32-echo train were sacrificed to incorporate the navigator projections. This could be avoided by inserting a gradient-echo projection navigator along the phase-encoded direction before the  $180^\circ$  pulse in each shot. Also, other types of navigator echoes could be used, such as low-resolution spiral scans, which might be better suited to locate the change than the projection navigators studied here.

A basic limitation of this technique, as well as other reduced FOV methods such as inner volume MRI (11,12), is the degradation of the SNR in the rFOV as a result of the limited sampling of k space. When updating

an rFOV consisting of one quarter of the full FOV, the SNR in the rFOV, as calculated by Hu and Parrish (6), is 2.65 times smaller than in the rest of the image. Aliasing artifact further degrades image quality in the rFOV and cannot be eliminated completely even with the use of navigator echoes.

Despite the limitations of the method, our results show that a fourfold improvement in temporal resolution can be obtained with sufficient image quality to resolve events that would otherwise be obscured by motion artifact if using the original rFOV method. The method produces T2-weighted dynamic image updates after each multi-echo shot. The common use of fast SE in abdominal imaging of the liver (13-15) and its efficiency to enhance contrast (16) and reduce motion artifacts (9) motivated our choice of the RARE sequence for our abdominal imaging experiments. Our method can be adapted readily to other multi-echo sequences such as gradient and spin echo (GRASE) (17,18).

Finally, a standard image update can still be reconstructed from a full k-space set after multiple shots, because our method only involves a particular ordering of the k-space acquisition from each shot, followed by a special method to reconstruct the dynamic updates. Therefore, no acquired image information is sacrificed using our method, and the fast dynamic update may be very useful for applications such as interventional MRI, in which improved temporal resolution is needed.

**Acknowledgments:** The authors thank Dr. Koichi Oshio for the use of his RARE pulse sequence code.

#### References

1. Matsumoto R, Oshio K, Jolesz FA. Monitoring of laser and freezing-induced ablation in the liver with T1-weighted MR imaging. *J Magn Reson Imaging* 1992; 2:555-562.
2. Fried MP, Jolesz FA. Image guided intervention for diagnosis and treatment of disorders of the head and neck. *Laryngoscope* 1993; 103:924-927.
3. Arbogast-Ranvier S, Gangi A, Choquet P, Brunot B, Constantinesco A. An in-vitro study at low field of MR guidance of a biopsy needle. *Magn Reson Imaging* 1995; 13:321-324.
4. Yamashita Y, Yoshimatsu S, Sumi M, Harada M, Takahashi M. Dynamic MR imaging of hepatoma treated by transcatheter arterial embolization therapy. *Acta Radiol* 1993; 34:303-308.
5. Panych LP, Jolesz FA. A dynamically adaptive imaging algorithm for wavelet encoded MRI. *Magn Reson Med* 1996 (in press).
6. Hu X, Parrish T. Reduction of the field of view for dynamic imaging. *Magn Reson Med* 1994; 31:691-694.
7. Kim WS, Mun CW, Kim DJ, Cho ZH. Extraction of cardiac and respiratory motion cycles by use of projection data and its applications to NMR imaging. *Magn Reson Med* 1990; 13:25-37.
8. Hennig J, Naureth A, Friedburg H. RARE imaging: a fast imaging method for clinical MR. *Magn Reson Med* 1986; 3:823-833.
9. Francis IR, Sigeti JS, Foo TKF, Low RN. Abdominal mr imaging: comparison of t2-weighted fast and conventional spin-echo, and contrast-enhanced fast multiplanar spoiled gradient-recalled imaging. *Radiology* 1993; 186:803-811.
10. Bailes DR, Gilderdale DJ, Bydder GM, Collins AG, Firmin DN. Respiratory ordered phase encoding (ROPE): a method for reducing respiratory motion artifacts in MR imaging. *J Comput Assist Tomogr* 1985; 9:835-838.
11. Feinberg DA, Hoenninger JC, Crooks LE, Kaufman L, Watts JC, Arkawa M. Inner volume MR imaging: technical concepts and their application. *Radiology* 1985; 156:743-747.
12. Oshio K, Mulkern RV. Rapid fat/water assessment in knee bone marrow with inner-volume RARE spectroscopic imaging. *J Magn Reson Imaging* 1992; 2:601-604.
13. Chien D, Mulkern RV. Fast spin-echo studies of contrast and small-lesion definition in a liver-metastasis phantom. *J Magn Reson Imaging* 1992; 2:483-487.
14. Naganawa S, Jenner G, Cooper TG, Potchen EJ, Ishigaki T. Rapid MR imaging of the liver: comparison of twelve techniques for single breath-hold whole volume acquisition. *Radiat Med* 1994; 12:255-261.
15. Reimer P, Jacobus F, Rummeny EJ, et al. Rapid spin echo sequences for detection and characterization of focal liver lesions. Use of fast t2-weighted spin echo with fat suppression and fast spin echo with combined gradient echo (GRASE). *Radiology* 1995; 35:911-918.
16. Schwartz LH, Seltzer SE, Tempany CM, et al. Prospective comparison of t2-weighted fast spin-echo, with and without fat suppression, and conventional spin-echo pulse sequence in the upper abdomen. *Radiology* 1993; 189:411-416.
17. Oshio K, Feinberg DA. Grase (gradient and spin-echo) imaging: a novel fast MRI technique. *Magn Reson Med* 1991; 20:344-349.
18. Feinberg DA, Oshio K. Grase (gradient and spin-echo) MR imaging: a new fast clinical imaging technique. *Radiology* 1991; 181:597-602.

**Publication:**

Paper II:

Multi-component Apparent Diffusion Coefficients in Human Brain: Relationship to Spin-Lattice Relaxation.

Authors:

Robert V. Mulkern, Hale Pinar Zengingonul, Richard L. Robertson, Peter Bogner, Kelly H. Zou, Hakon Gubdjartsson, Charles R.G. Guttmann, David Holtzman, **Walid Kyriakos**, Ferenc A. Jolesz, and Stephan E. Maier.

Journal:

Magnetic Resonance in Medicine (MRM)  
44: 292 – 300, 2000.

# Multi-component Apparent Diffusion Coefficients in Human Brain: Relationship to Spin-Lattice Relaxation

Robert V. Mulkern,<sup>1,2\*</sup> Hale Pinar Zengingonul,<sup>2</sup> Richard L. Robertson,<sup>1</sup> Peter Bogner,<sup>3</sup> Kelly H. Zou,<sup>2</sup> Hakon Gudbjartsson,<sup>4</sup> Charles R.G. Guttman,<sup>2</sup> David Holtzman,<sup>2</sup> Walid Kyriakos,<sup>1</sup> Ferenc A. Jolesz,<sup>2</sup> and Stephan E. Maier<sup>2</sup>

**In vivo measurements of the human brain tissue water signal decay with b-factor over an extended b-factor range up to 6,000 s/mm<sup>2</sup> reveal a nonmonoexponential decay behavior for both gray and white matter. Biexponential parametrization of the decay curves from cortical gray (CG) and white matter voxels from the internal capsule (IC) of healthy adult volunteers describes the decay process and serves to differentiate between these two tissues. Inversion recovery experiments performed in conjunction with the extended b-factor signal decay measurements are used to make separate measurements of the spin-lattice relaxation times of the fast and slow apparent diffusion coefficient (ADC) components. Differences between the spin-lattice relaxation times of the fast and slow ADC components were not statistically significant in either the CG or IC voxels. It is possible that the two ADC components observed from the extended b-factor measurements arise from two distinct water compartments with different intrinsic diffusion coefficients. If so, then the relaxation results are consistent with two possibilities. Either the spin-lattice relaxation times within the compartments are similar or the rate of water exchange between compartments is "fast" enough to ensure volume averaged  $T_1$  relaxation yet "slow" enough to allow for the observation of biexponential ADC decay curves over an extended b-factor range. Magn Reson Med 44:292-300, 2000. © 2000 Wiley-Liss, Inc.**

**Key words:** apparent diffusion coefficient; brain; biexponential decay; spin-lattice relaxation

Diffusion imaging is playing an increasingly important diagnostic role due to its extreme sensitivity to acute stroke in comparison with conventional  $T_1$ - and  $T_2$ -weighted imaging (1-3). Due to the effects of anisotropic diffusion (4,5), it is now generally realized that at least three directions of the diffusion sensitization gradient should be sampled to generate trace images free from the effects of preferred directional diffusion. Indeed a minimum of 6 directions must be sampled if a full diffusion tensor for each voxel is to be evaluated (6-8) for studies of myelin development and brain microarchitecture (9,10). Thus, the current trend towards clinical implementation of diffusion imaging is to sample multiple slices of the brain each at a low and a high b-factor, the latter being

typically on the order of 1,000 s/mm<sup>2</sup>, and to repeat the high b-factor sampling for at least three and up to six directions of the diffusion sensitization gradient.

To this inherent complexity of brain tissue water diffusion measurement and interpretation, yet another complicating factor has recently emerged. Namely, when sampled over an extended b-factor range much larger than typically used clinically, the brain water signal decay in vivo from both rats and humans does not display the monoexponential signal decay so commonly assumed (11,12). Indeed a bi- as opposed to monoexponential model of decay is required to fit the ADC decay data. This finding is not explainable within the confines of the diffusion tensor formalism alone. Furthermore, the extended b-factor range required for observing and measuring the biexponential decay is readily accessible with conventional scanners using long echo times and standard gradient strengths of 1 Gauss/cm. This endows the finding with significant clinical ramifications and motivates further studies designed to explore the nature of the nonmonoexponential brain water signal decay.

In this work, the spin-lattice relaxation behavior of human brain water signal decay over an extended b-factor range was examined by combining multi-b-factor sampling techniques with inversion recovery methods. Voxels from internal capsule (IC) white matter and cortical gray (CG) matter were sampled to determine relaxation in tissues with and without anisotropic diffusion effects. The spin-lattice relaxation times of the fast and slow ADC components, evaluated on the basis of biexponential ADC decomposition as a function of inversion time, were found to be quite similar in either voxel type. Similarly,  $T_1$  values evaluated directly from the data without the use of biexponential decompositions showed no systematic dependence on b-factor over the range sampled. Implications of these results are discussed within the context of a two-compartment model for explaining the observed biexponential ADC behavior of brain water signal decay over extended b-factor ranges in both gray and white matter.

## MATERIALS AND METHODS

### Data Acquisition

All studies were performed with a 1.5 T Signa scanner (General Electric Medical Systems, Milwaukee, WI) operating at the 5.4 hardware/software configuration using a quadrature head coil. Eight healthy adult volunteers ranging from 24 to 38 years of age participated in the study, providing informed consent according to the rules of the institutional review board. A set of 10-mm thick axial

<sup>1</sup>Department of Radiology, Children's Hospital, Harvard Medical School, Boston, Massachusetts.

<sup>2</sup>Department of Radiology, Brigham and Women's Hospital, Harvard Medical School, Boston, Massachusetts.

<sup>3</sup>Diagnostic Center, Pannon University of Agriculture, Kaposvar, Hungary.

<sup>4</sup>deCCDE Genetics, Inc., Reykjavik, Iceland.

\*Correspondence to: Robert V. Mulkern, Department of Radiology, Children's Hospital, 300 Longwood Avenue, Boston, MA 02115.  
E-mail: mulkern@bwh.harvard.edu

Received 4 March 1999; revised 21 March 2000; accepted 30 March 2000.

$T_1$ -weighted spin echo images (TR/TE = 500/20) were initially acquired. From these images, a  $15 \times 15 \text{ mm}^2$  cross-sectional column extending left-to-right and passing through cortex and white matter of the internal capsule at the level of the third ventricle was chosen for interrogation. Detailed diffusion measurements of this tissue column were then performed using an inner volume spin-echo sequence as described in a previous study (12) but modified to incorporate inversion pulses for  $T_1$  measurement. Mutually orthogonal slice selective excitation and refocusing pulses were used to solicit an echo from the intersection of the two slices. The inversion pulse was identical to the slice selective refocusing pulse of the spin echo sequence. Standard frequency encoding was performed for along-column spatial mapping to obtain a 1D image of the column every repetition time TR. A receiver bandwidth of 6 kHz, 128 frequency encoding steps, and a column length of 24 cm were used to obtain an along-column spatial resolution of 1.9 mm. A long echo time of 175 msec was employed to accommodate heavy diffusion weighting with long duration Stejskal-Tanner pulsed field gradients placed about the refocusing pulse. All three gradient axes were used for diffusion sensitization in a (1,1,1) configuration. The amplitudes  $G$  of the diffusion sensitization gradients were incremented each TR period to cover a wide range of b-factors from 5 to 6,000  $\text{s/mm}^2$  in 48 equal steps. The maximum gradient strength available along each direction was 1 Gauss/cm and the b-factor was calculated through the relation

$$b = 3(\delta\gamma G)^2(\Delta - \delta/3) \quad [1]$$

in which  $\delta$  is the duration of each diffusion gradient lobe and  $\Delta$  is the time between their leading edges, which were 79.6 and 82.9 msec, respectively. The factor of 3 in (1) accounts for the use of all three gradients simultaneously for diffusion sensitization. A 3-sec TR was used to obtain 48 b-factor data sets of the tissue column in 2.5 min, a scan time that includes 2 "dummy" acquisitions to set the system in steady state prior to data collection. Data sets were first acquired without an inversion pulse and then with an inversion pulse at 8 separate inversion times (TI) of 50, 100, 150, 200, 250, 300, 350, and 400 msec prior to each excitation.

#### Data Analysis

The signal decay with b-factor from  $0.19 \times 1.5 \times 1.5 \text{ cm}^3$  voxels along the tissue column through the brain were available for analysis. We averaged two adjacent voxels along the column in an area of cortical gray matter (CG) and in an area of white matter in the left internal capsule (IC) to extract decay curves from 0.84 mL voxels in these two regions for each volunteer. The CG and IC decay curves were then fit with a biexponential function of the form

$$SI = A_1 \exp(-D_1 b) + A_2 \exp(-D_2 b) \quad [2]$$

where SI is the signal intensity at b-factor  $b$ ,  $A_1$  and  $A_2$  are the amplitudes and  $D_1$  and  $D_2$  are the diffusion coefficients of the fast and slow diffusing components, respectively.

Fitting was performed using a Marquardt-Levenberg algorithm, as described previously (13). For the smallest b-factor of 5  $\text{s/mm}^2$  and occasionally for the second smallest b-factor of 133  $\text{s/mm}^2$ , signal intensities were obviously affected by a component with an ADC greater than that of pure water at 37°C. Such behavior at the lowest b-factors is attributed to the small combined CSF/perfusion pool reported previously (14,15). Data from the lowest b-factor, and occasionally the second lowest, were thus excluded from the biexponential fitting process to avoid contamination from this pool, which is estimated to have a negligible contribution to signal decay at b-factors above 300  $\text{s/mm}^2$ . From the baseline data acquired with no inversion pulse, differences in the biexponential parameters between CG and IC data were determined by Student's paired t-test with  $P$  values  $< 0.01$  considered significant (16). The appropriateness of the t-test was verified by demonstrating a normal distribution of differences using the z-test (17) as written in S-PLUS (18).

A Bloch equation analysis of the spin echo inversion recovery experiment reveals that for a system with equilibrium magnetization  $M_0$ , the steady state  $T_1$ -weighting immediately after the 90° excitation pulse is given by

$$S = M_0 [1 - 2 \exp(-TI/T_1) - \exp(-TR/T_1) + 2 \exp(-TR/T_1) \exp(TE/(2T_1))] \quad [3]$$

The latter two terms combine destructively and are easily shown to be negligible for  $T_1$  and TR values on the order of 1 and 3 sec, respectively. This being the case for our experiments (vide infra), we drop the last two terms in (3) and rearrange the remaining terms to obtain a quantity  $\Psi$  suitable for log-linear regression analysis of  $T_1$  relaxation:

$$\Psi = (M_0 - S)/(2M_0) = \exp(-TI/T_1) \quad [4]$$

where the  $M_0$  values are ADC component amplitudes determined from baseline data sets acquired with no inversion pulse. Preliminary experiments performed with TI values from 50 msec to 2 sec revealed signal minima for TI values between 600 and 800 msec (data not shown). Thus, the use of TI values less than 400 msec ensures that the  $S$  in Eq. [4] is technically negative for operational use. Both the fast and slow ADC component amplitudes  $A_1$  and  $A_2$  were used in Eq. [4] to obtain experimental measures of  $\Psi$  for each separate ADC component. The natural logarithm of  $\Psi$  vs TI was fit by linear regression and the slopes used to obtain the spin-lattice relaxation times for the fast and slow ADC components  $T_{1f}$  and  $T_{1s}$ , respectively. Correlation coefficients for each fit were also obtained from the linear regression analyses. Statistically significant differences between  $T_{1f}$  and  $T_{1s}$  for the CG and IC data were determined using Student's paired t-tests with  $P$  values  $< 0.01$  considered significant. The appropriateness of the t-test was verified by demonstrating a normal distribution of differences using the z-test (17) as written in S-PLUS (18). This approach of finding the separate  $T_1$ s for the fast and slow ADC components is necessarily linked to the assumption of a biexponential model since the amplitudes of the biexponential fits are used for the inversion recovery analysis. For an evaluation of  $T_1$  relaxation behavior

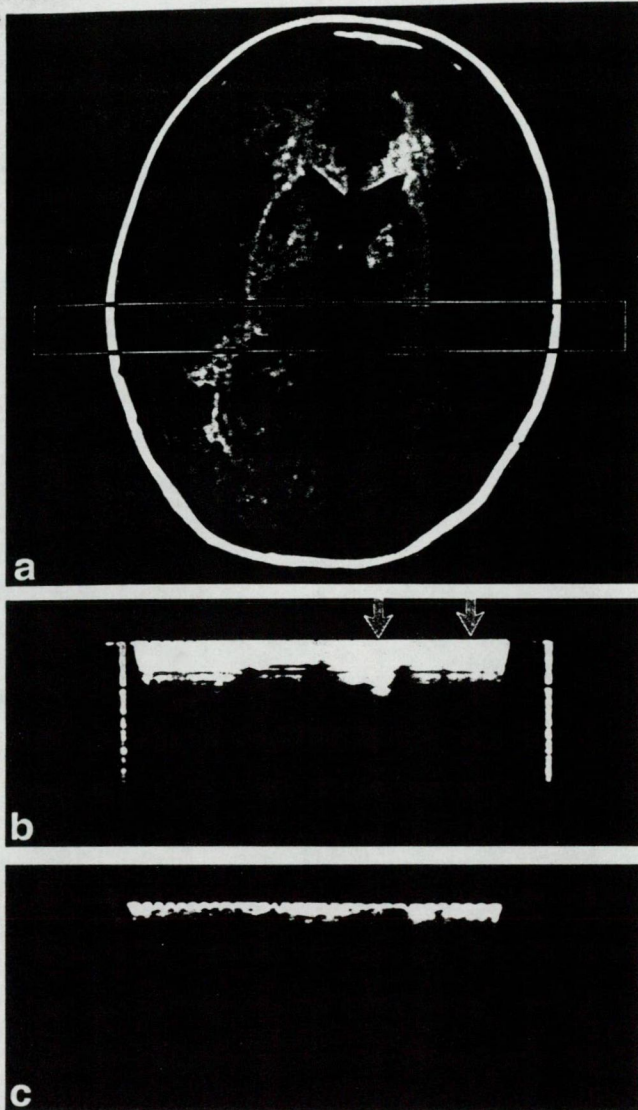


FIG. 1. **a:**  $T_1$ -weighted image depicting the tissue column ( $15 \times 15 \text{ mm}^2$  cross-section) targeted for multi-component ADC study. **b:** Image of the column at 48 b-factors from 5 to 6000  $\text{s/mm}^2$  (top to bottom) as acquired with no inversion pulse. Arrows denote the two locations sampled for statistical analyses in each of the 8 volunteers. **c:** Same as in **b** but with each acquisition preceded by an inversion pulse at a TI of 250 msec.

which is independent of the biexponential model and associated fits,  $S$  values as a function of TI at 7 equally spaced b-factors from 515 to 5,107  $\text{s/mm}^2$  were subjected to the inversion recovery analysis to obtain  $T_1$  values as a function of b-factor.

## RESULTS

Figure 1a shows a representative tissue column selected for ADC measurement. Figure 1b and c are one-dimensional images of the column at 48 b-factors ranging from 5 to 6,000  $\text{s/mm}^2$  (top to bottom) as scanned without an inversion pulse (**b**) and with an inversion pulse at a TI of 250 msec (**c**). The latter two images have been filmed with identical window levels so that the signal loss due to  $T_1$

relaxation over the 250-msec inversion time can be appreciated. Arrows in Fig. 1b indicate the two horizontal locations along the column from which signal decay curves were extracted, representing 0.84-mL voxels in the cortical gray (CG) matter and the left internal capsule (IC). The latter consistently appeared as a prominent vertical streak in all cases, presumably due to slow diffusion processes in the white matter tracts with the (1,1,1) diffusion sensitization gradient configuration.

Figure 2a and b are signal decay curves extracted from the CG and IC voxels, respectively, taken from the data sets of Fig. 1. The curvature of the decay curves on these semi-log plots indicates nonmonoexponential behavior for signal intensities well above the baseline noise levels plotted at the bottom of each figure. The decay curves are well characterized with biexponential functions as evidenced by the solid lines through the experimental data points obtained from fits to Eq. [2]. In general, the  $\chi^2$  values

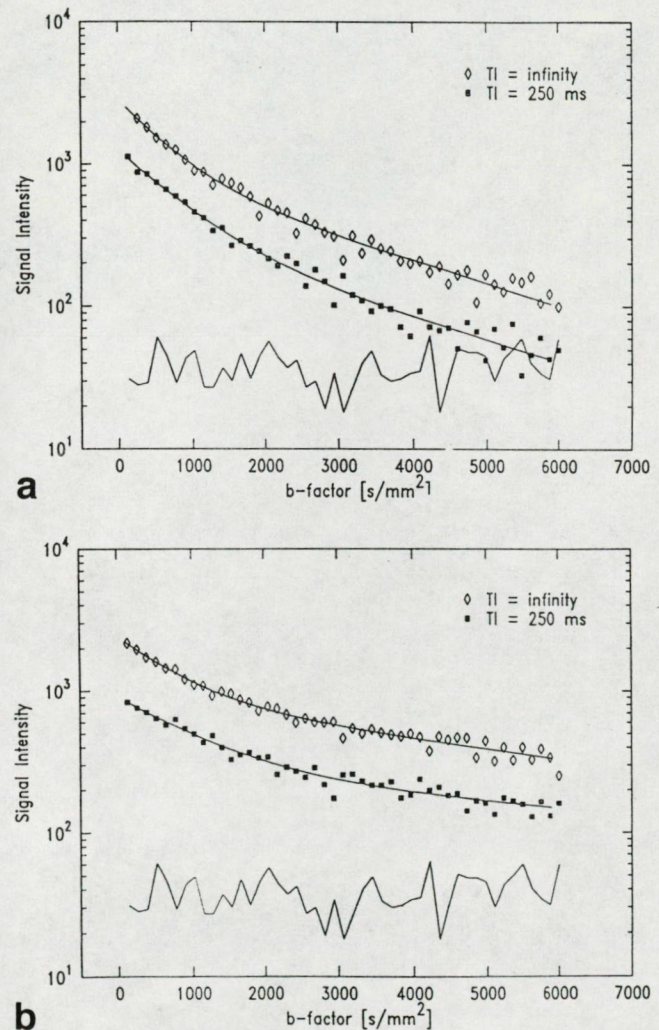


FIG. 2. **a:** Brain tissue water signal vs. b-factor as taken from a voxel in the cortical gray (CG) matter using no inversion pulse (TI = infinity) and an inversion pulse at TI = 250 msec. Shown through the data are the biexponential fits obtained with the Marquardt-Levenberg algorithm (solid lines). Baseline noise values are plotted at the bottom of the figure. **b:** Same as in **a** but for a voxel in the internal capsule (IC).

Table 1  
Interindividual Means and Standard Deviations (N = 8) of the Biexponential Parameters Obtained From Baseline Data Sets (No Inversion Pulse) From Voxels in the Cortical Gray (CG) and Internal Capsule (IC) White Matter

	$A_1/(A_1 + A_2)$	$D_1$ ( $\mu\text{m}^2/\text{ms}$ )	$D_2$ ( $\mu\text{m}^2/\text{ms}$ )
CG	$0.73 \pm 0.03$	$1.46 \pm 0.33$	$0.32 \pm 0.09$
IC	$0.66 \pm 0.03$	$1.02 \pm 0.22$	$0.11 \pm 0.03$

obtained from biexponential fits of the data were 5 to 10 times smaller than  $\chi^2$  values obtained from monoexponential fits, which were clearly inappropriate over this extended b-factor range.

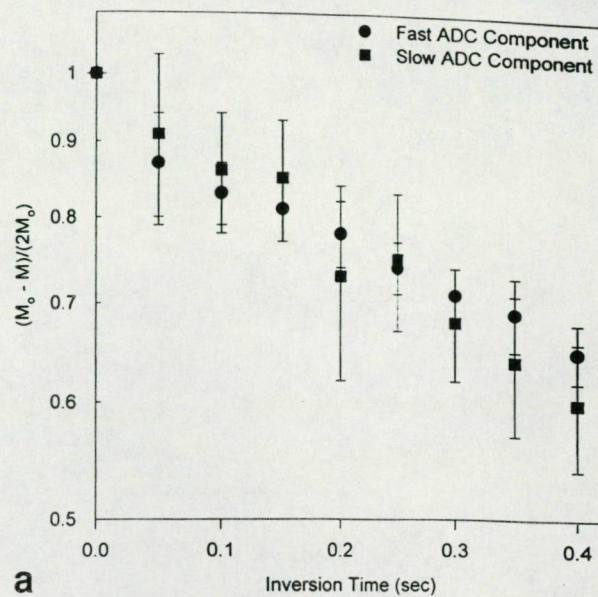
Table 1 shows interindividual means and standard deviations of the biexponential parameters found from fitting the baseline CG and IC decay curves acquired without any inversion pulse. The fraction of the fast diffusion component  $A_1/(A_1 + A_2)$  was significantly smaller in the IC than in the CG ( $P < 0.01$ ). Similarly, the value of the slow diffusion coefficient  $D_2$ , was significantly smaller in the IC than in the CG ( $P < 0.01$ ). The interindividual means and standard deviations of  $\Psi$  (see Eq. [4]) were evaluated at each TI for each ADC component from all 8 volunteers. The composite relaxation curves for the fast and slow ADC components, as found for the CG and IC data, are shown in Fig. 3a and b. A monotonic decrease with TI is observed on these semi-log plots. The inter-individual mean correlation coefficients obtained from linear fits of the CG data were  $0.97 \pm 0.05$  (fast component) and  $0.86 \pm 0.09$  (slow component), whereas for the IC data they were  $0.96 \pm 0.06$  (fast component) and  $0.90 \pm 0.11$  (slow component). Table 2 provides the interindividual means and standard deviations (N = 8) for the fast and slow spin-lattice relaxation times of the CG and IC. There was not a statistically significant difference between  $T_{1f}$  and  $T_{1s}$  in either the CG or the IC ( $P > 0.20$ ). The  $T_{1f}$  and  $T_{1s}$  values were smaller in the IC than in the CG, as expected for white vs. gray matter in adults (19). The difference in the  $T_{1f}$  values for the IC and CG achieved statistical significance ( $P < 0.01$ ).

Figure 4a and b shows composite plots made from all 8 volunteers of the fast and slow diffusion coefficient values obtained at each TI for the CG and IC data sets, respectively. There is little variation of the measured diffusion coefficients with TI, indicating robust biexponential fits even as the overall signal-to-noise decreased with the lengthening of TI. The decreased value of the slow diffusion coefficient in the IC compared to the CG by nearly a factor of 3, as found from the baseline data and reported in Table 1, is seen to hold regardless of the TI value.

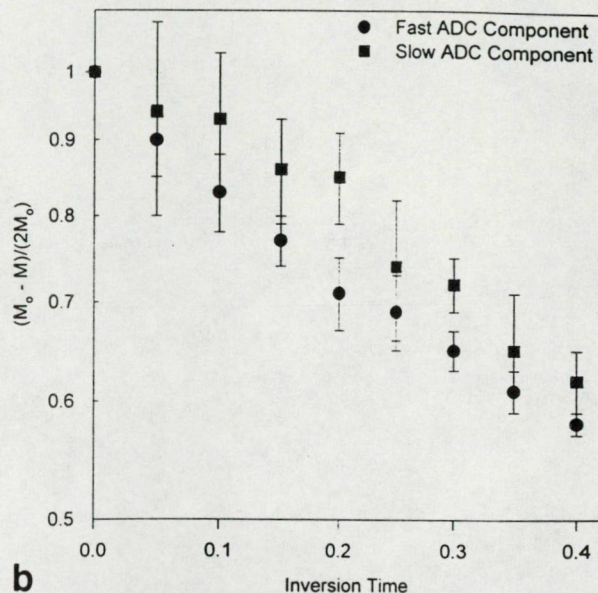
Figure 5 shows the inter-individual mean  $T_1$  values evaluated directly from signal intensities at 7 different b-factors over the full range. The IC  $T_1$  values are generally lower than the CG values at all b-factors and the mean values of  $981 \pm 46$  msec for the CG and  $849 \pm 51$  msec are in general agreement with the values reported in Table 2 obtained using the biexponential model. The figure demonstrates the relative independence of the  $T_1$  measurement over the extended b-factor range sampled.

**DISCUSSION**

Brain tissue water signal decay with b-factor departs from the monoexponential behavior commonly assumed when



**a**



**b**

FIG. 3. a: Composite plot of the spin-lattice relaxation decay for the fast and slow ADC component amplitudes (see Eq. [4]) as a function of inversion time for the CG voxels sampled in all 8 volunteers (mean  $\pm$  SD). As in a but for the IC voxels.

generating ADC maps in clinical practice once the b-factor range is extended towards  $6,000 \text{ s/mm}^2$ . The curvature of the brain ADC decay curves (Fig. 2) generally becomes noticeable for b-factors above  $2000 \text{ s/mm}^2$  regardless of

Table 2  
Interindividual Means and Standard Deviations (N = 8) of the Spin-Lattice Relaxation Times Found for the Fast and Slow Diffusing ADC Components in Cortical Gray (CG) and Internal Capsule (IC) Voxels

	$T_{1f}$ (s)	$T_{1s}$ (s)
CG	$1.08 \pm 0.10$	$0.98 \pm 0.26$
IC	$0.77 \pm 0.05$	$0.85 \pm 0.14$

Table 1  
Interindividual Means and Standard Deviations (N = 8) of the Biexponential Parameters Obtained From Baseline Data Sets (No Inversion Pulse) From Voxels in the Cortical Gray (CG) and Internal Capsule (IC) White Matter

	$A_1/(A_1 + A_2)$	$D_1 (\mu\text{m}^2/\text{ms})$	$D_2 (\mu\text{m}^2/\text{ms})$
CG	$0.73 \pm 0.03$	$1.46 \pm 0.33$	$0.32 \pm 0.09$
IC	$0.66 \pm 0.03$	$1.02 \pm 0.22$	$0.11 \pm 0.03$

obtained from biexponential fits of the data were 5 to 10 times smaller than  $\chi^2$  values obtained from monoexponential fits, which were clearly inappropriate over this extended b-factor range.

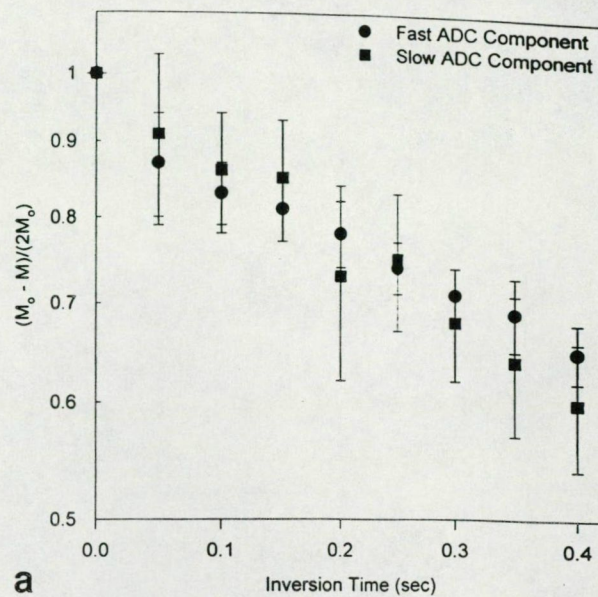
Table 1 shows interindividual means and standard deviations of the biexponential parameters found from fitting the baseline CG and IC decay curves acquired without any inversion pulse. The fraction of the fast diffusion component  $A_1/(A_1 + A_2)$  was significantly smaller in the IC than in the CG ( $P < 0.01$ ). Similarly, the value of the slow diffusion coefficient  $D_2$ , was significantly smaller in the IC than in the CG ( $P < 0.01$ ). The interindividual means and standard deviations of  $\Psi$  (see Eq. [4]) were evaluated at each TI for each ADC component from all 8 volunteers. The composite relaxation curves for the fast and slow ADC components, as found for the CG and IC data, are shown in Fig. 3a and b. A monotonic decrease with TI is observed on these semi-log plots. The inter-individual mean correlation coefficients obtained from linear fits of the CG data were  $0.97 \pm 0.05$  (fast component) and  $0.86 \pm 0.09$  (slow component), whereas for the IC data they were  $0.96 \pm 0.06$  (fast component) and  $0.90 \pm 0.11$  (slow component). Table 2 provides the interindividual means and standard deviations (N = 8) for the fast and slow spin-lattice relaxation times of the CG and IC. There was not a statistically significant difference between  $T_{1f}$  and  $T_{1s}$  in either the CG or the IC ( $P > 0.20$ ). The  $T_{1f}$  and  $T_{1s}$  values were smaller in the IC than in the CG, as expected for white vs. gray matter in adults (19). The difference in the  $T_{1f}$  values for the IC and CG achieved statistical significance ( $P < 0.01$ ).

Figure 4a and b shows composite plots made from all 8 volunteers of the fast and slow diffusion coefficient values obtained at each TI for the CG and IC data sets, respectively. There is little variation of the measured diffusion coefficients with TI, indicating robust biexponential fits even as the overall signal-to-noise decreased with the lengthening of TI. The decreased value of the slow diffusion coefficient in the IC compared to the CG by nearly a factor of 3, as found from the baseline data and reported in Table 1, is seen to hold regardless of the TI value.

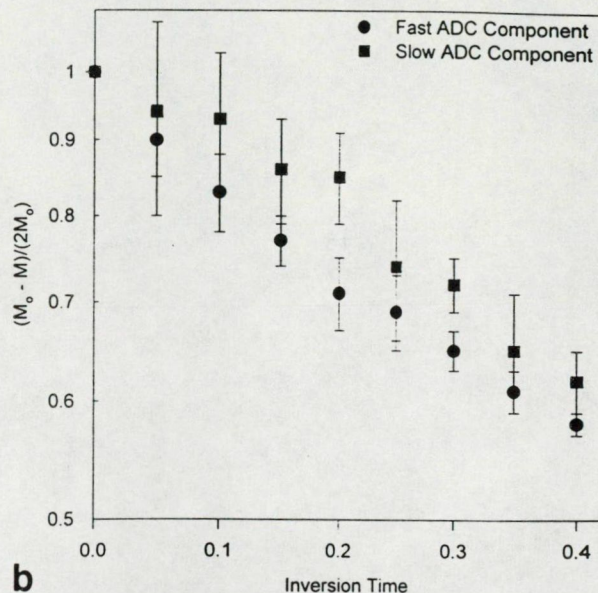
Figure 5 shows the inter-individual mean  $T_1$  values evaluated directly from signal intensities at 7 different b-factors over the full range. The IC  $T_1$  values are generally lower than the CG values at all b-factors and the mean values of  $981 \pm 46$  msec for the CG and  $849 \pm 51$  msec are in general agreement with the values reported in Table 2 obtained using the biexponential model. The figure demonstrates the relative independence of the  $T_1$  measurement over the extended b-factor range sampled.

**DISCUSSION**

Brain tissue water signal decay with b-factor departs from the monoexponential behavior commonly assumed when



a



b

FIG. 3. a: Composite plot of the spin-lattice relaxation decay for the fast and slow ADC component amplitudes (see Eq. [4]) as a function of inversion time for the CG voxels sampled in all 8 volunteers (mean  $\pm$  SD). As in a but for the IC voxels.

generating ADC maps in clinical practice once the b-factor range is extended towards  $6,000 \text{ s/mm}^2$ . The curvature of the brain ADC decay curves (Fig. 2) generally becomes noticeable for b-factors above  $2000 \text{ s/mm}^2$  regardless of

Table 2  
Interindividual Means and Standard Deviations (N = 8) of the Spin-Lattice Relaxation Times Found for the Fast and Slow Diffusing ADC Components in Cortical Gray (CG) and Internal Capsule (IC) Voxels

	$T_{1f}$ (s)	$T_{1s}$ (s)
CG	$1.08 \pm 0.10$	$0.98 \pm 0.26$
IC	$0.77 \pm 0.05$	$0.85 \pm 0.14$

diffusion at semi-permeable boundaries was accounted for in a manner similar to that proposed by Stanisz et al. in detailed ADC studies of bovine optic nerve *in vitro* (27,28). Aside from *in vitro* studies, the intra- and extracellular water diffusion model is commonly invoked in brain ADC imaging studies of stroke where typically only two or at most a few b-factors under 2000 s/mm<sup>2</sup> are sampled, necessitating monoexponential decay analyses. For instance, van Gelderen et al. (29) performed ADC imaging of acute stroke in cats and observed an ADC decrease from 0.65  $\mu\text{m}^2/\text{msec}$  in normal brain to 0.42  $\mu\text{m}^2/\text{msec}$  in acute stroke. The observed ADC decrease was attributed to intracellular swelling that was quantitatively consistent with a volume averaged fast exchange model for the ADC as based on literature values of intra- and extracellular volume ratios in normal and ischemic adult brain tissue.

Niendorf et al. (11) reported biexponential ADC behavior in *in vivo* rat brains. At 4.7 T they employed a single voxel PRESS technique to measure rat brain tissue water signal decay over an extended b-factor range up to 10,000 s/mm<sup>2</sup>. In normal adult rat brain, they reported a 0.80 volume fraction for the fast ADC component, which dropped to 0.69 postmortem. The immature rat brain *in vivo* had an even higher fast ADC component fraction than the adult brain, 0.90 vs. 0.80, respectively, consistent with a larger extracellular space in the immature brain. Changes of the intracellular volume fraction made on the basis of electrical impedance measurements were shown to correlate well with changes of the fraction of the slow ADC component observed during recovery from excitotoxic brain edema. All of these observations are consistent with an intra- vs. extracellular model interpretation for the slow and fast ADC components. A confounding feature noted by these investigators, however, was a discrepancy between the ADC component volume fractions and literature values for the actual intracellular and extracellular water volume fractions in normal adult brain that are approximately 0.8 and 0.2, respectively. Thus, we might anticipate the slow, intracellular, ADC component to have a larger fraction than the fast, extracellular, ADC component, opposite to what is actually observed. More recently, Buckley et al. reported the effects of ouabain on multi-component ADC behavior in perfused rat brain slice preparations studied at high field (30). These investigators interpreted their findings in terms of the intra- and extracellular compartmentation model for the biexponential ADC behavior when measured over an extended b-factor range up to 4,500 s/mm<sup>2</sup>. The ouabain demonstrated the predicted effect of cell swelling, as inferred from the increase in the relative amplitude of the slow ADC component if associated with the intracellular water compartment. As with Niendorff et al. (11), however, these authors also found a larger fast than slow ADC component fraction. They argued that  $T_2$ -weighting of the data obtained with the spin-echo technique favors a larger fraction of signal from extracellular water, thus reversing the expected rank order of the observed volume fractions (30).

Our ability to separate two ADC components on the basis of multi-b-factor measurements allows us to probe the individual magnetic environments of each component. In this study, inversion recovery experiments were combined with multi-b-factor measurements in order to deter-

mine the spin-lattice relaxation properties of the two ADC components. The experimental evidence suggests that there is no statistically significant difference between the spin-lattice relaxation times of the two ADC components observed in our studies (Table 2). The values of the fast and slow diffusion coefficients were well-behaved with respect to variations of the inversion time (Fig. 4a and b) whereas the amplitudes of the two ADC components were well-suited to log-linear regression analyses within the available signal-to-noise limitations (Fig. 3a and b). An alternate analysis of the data, free from the biexponential fitting routine, was also used to show that the spin-lattice relaxation behavior was independent of b-factor (Fig. 5). Several possibilities for the interpretation of the non-exponential behavior of brain water signal decay with b-factor which are consistent with these  $T_1$  results are now presented.

One possibility is that there are two compartments with different intrinsic diffusion coefficients with no water exchange between the compartments. In this case, we would have to conclude that the two compartments have very similar spin-lattice relaxation times. This would be somewhat surprising since an environment with a very small diffusion coefficient suggests multiple interactions between water and other biological constituents, macromolecules, cellular organelles, etc. These interactions would tend to enhance spin-lattice relaxation, reducing the  $T_1$  compared to water in the compartment with fewer interactions. A second possibility which we demonstrate is also compatible with the experimental findings is to assume that there is a moderate exchange of water between the two compartments which is fast enough to insure a well-mixed spin-lattice relaxation behavior (fast exchange) but slow enough to allow for the observation of biexponential like ADC behavior (intermediate exchange).  $T_1$  values in tissue are fairly long, 400 to 2000 msec, for example. Thus, it is easy to show using the Zimmerman-Britton two-site exchange equations (31) provided in the appendix that with even moderate exchange rates on the order of 5 to 10 Hz, the  $T_1$  relaxation of a two-component system is expected to be in the fast exchange regime. For instance let us assume an intracellular volume fraction of 0.8, an intracellular spin-lattice relaxation rate of 1.5  $\text{sec}^{-1}$  and an extracellular relaxation rate of 0.5  $\text{sec}^{-1}$ . The plot in Figure 6 shows the fractional amplitudes of the slow and fast relaxing components (solid and dashed-dotted line, respectively) of the anticipated biexponential  $T_1$  relaxation curve as a function of the exchange rate  $k_{12}$  from the extra- to intracellular space. Beyond a  $k_{12}$  of approximately 4  $\text{sec}^{-1}$ , the biexponential collapses to a single component whose relaxation rate is equal to the volume averaged "fast exchange" limit.

With such exchange rates the ADC decay curves measured over the b-factor ranges we have sampled should still be biexponential in form. This is demonstrated using the relations proposed by Karger et al. (32) to simulate the signal decay with b-factor from a two-compartment system in exchange. The equations are provided in the appendix and Fig. 7 shows three simulated ADC decay curves based upon them. The solid line is an ADC decay for the case of no exchange as generated using the mean biexponential parameters found for the CG voxels (Table 1). This curve

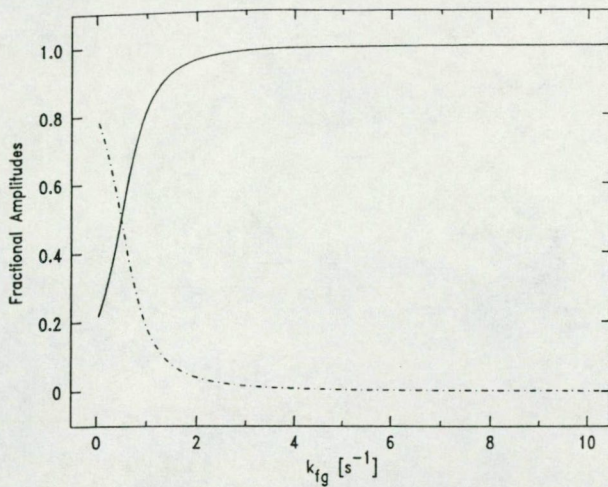


FIG. 6. Fractional amplitudes of the fast and slow relaxing components of the biexponential function describing spin-lattice relaxation as a function of exchange rate  $k_{fg}$ , for a two-site exchange system with volume fractions and intrinsic relaxation rates set to values expected for intracellular and extracellular brain tissue water.

implies that 73% of the water in brain CG voxels arises from a compartment with an intrinsic diffusion coefficient of  $1.46 \text{ } \mu\text{m}^2/\text{msec}$  and the remainder arises from a compartment with a slower diffusion coefficient of  $0.32 \text{ } \mu\text{m}^2/\text{msec}$ . As noted above, the relative percentages of these fractions are largely opposite that which would be expected on the basis of known extracellular and intracellular water volume percentages in brain tissue. The dashed line in Fig. 7 shows an ADC decay simulation from a system with a fast ADC component having a smaller fractional size than the slow diffusing ADC component, 0.4 vs. 0.6, respectively, which more closely resembles extra- and intracellular volume fractions in brain. The experimental settings  $\delta$ ,  $\Delta$ , and diffusion gradient strength maxima used in the Karger relations to generate this curve were the same as those we used experimentally (80 msec, 83 msec, and 1 Gauss/cm, respectively). A moderate exchange rate of 10 Hz from the smaller compartment to the larger compartment has been introduced and the intrinsic diffusion coefficient of the fast ADC component was approximately doubled to  $3.0 \text{ } \mu\text{m}^2/\text{msec}$  compared to the no exchange case. As may be seen, there is little noticeable difference between the no exchange case (solid line) and the moderate exchange case (dashed line) over the b-factor range sampled. Both curves display markedly nonexponential behavior well-suited to biexponential modeling. Because the Karger relations were derived with the simplifying assumption that  $\delta \ll \Delta$ , we also generated a hypothetical curve (diamonds) with the same two-site exchange rates, volume fractions, diffusion coefficients and  $\Delta$  value used for the dashed line curve. The gradient pulse width  $\delta$ , however, was reduced to 8 msec and the gradient maxima were set to 8.2 Gauss/cm in order to cover the same b-factor range. This curve demonstrates that even within the regime more suited for the use of the Karger relations, biexponential ADC behavior is still anticipated at moderate exchange rates which would eliminate any detectable  $T_1$  differences between ADC compartments.

Though two possibilities within the framework of the two-site exchange model have been forwarded, which are consistent with our  $T_1$  data, a third possibility is simply that the non-exponential signal decay is a manifestation of restricted diffusion processes which are only indirectly associated with biophysical compartmentation of water. Assaf and Cohen (33) recently studied the N-acetyl aspartate (NAA) proton resonance at 2.0 ppm in rat brains in vivo and reported biexponential ADC behavior over an extended b-factor range. Because the NAA molecule is exclusively intracellular, an interpretation of intra- vs. extracellular compartmentation cannot be invoked in this case. The authors suggested that their finding may represent a population of NAA molecules in the neuronal cell body and another population in the neuritic space consisting of axons and proximal dendrites. This hypothesis is consistent with the different sizes of the restriction to diffusion they estimated for each ADC component. In another study, Helmer et al. demonstrated nonmonoexponential behavior in water saturated samples of packed polystyrene beads (34). These authors discussed their results in terms of a porous media model in which the shapes of the actual decay curves are sensitive to features like the surface-to-volume ratios of the pores (34–36). Finally, a very recent study by Peled et al. (37) of in vitro water diffusion in frog sciatic nerve demonstrated how restricted diffusion effects within a collection of parallel solid cylinders with a distribution of axonal radii similar to that measured by independent means can quite readily result in ADC decay curves that appear “biexponential.”

Thus, it is clear that there are competing interpretations for nonmonoexponential ADC decay curves in brain and other materials with complex micro-topologies for water diffusion. Only further studies will permit more definitive conclusions to be drawn regarding multicomponent brain ADC behavior. It is, of course, appealing to interpret our results in terms of the intra- and extracellular water compartmentation model because a quantifiable separation of these compartments on the basis of other MR parameters has remained elusive. In this regard, attempts based on

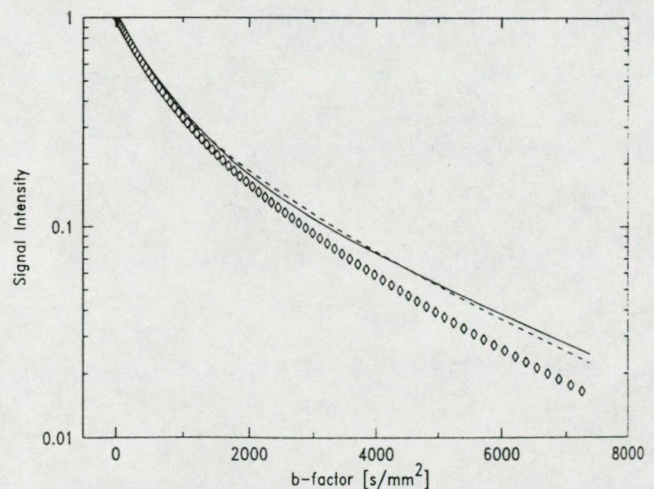


FIG. 7. Simulated signal decays with b-factor resulting from a two compartment system for different parameter settings, see text for details.

relaxation measurements in brain appear quite limited. The separation of cerebrospinal fluid (CSF) from brain parenchyma can apparently be performed with multi-echo imaging experiments based on significant differences in  $T_2$  values (38,39). Also, quantitation of a short  $T_2$  component associated with water between myelin sheaths in white matter ( $T_2$  between 10 and 30 ms) appears feasible using specialized Carr-Purcell-Meiboom-Gill (CPMG) imaging sequences (40). Though interesting from their own perspectives, these relaxation based measurements do not appear to reflect intra- and extracellular water volumes in brain. Thus, separating intra- and extracellular volume fractions in brain parenchyma in vivo using multi-component ADC analyses, even if corrections for  $T_2$  decay and exchange are required, remains an exciting possibility that may have important clinical ramifications in the diagnosis and management of neurological disease.

## CONCLUSIONS

The primary experimental finding reported is the lack of any significant difference between the fast and slow ADC component spin-lattice relaxation times in either gray (CG) or white matter (IC) voxels. If a two compartment model is assumed, then the implications are that there is no difference in the intrinsic  $T_1$  values within the two compartments or that exchange between the two compartments is fast enough to insure a single well-mixed  $T_1$  yet slow enough to allow for the separation of two separate ADC components. The latter explanation seems more likely and it has been demonstrated that moderate exchange rates from the fast ADC compartment to the slow ADC compartment would suffice to eliminate any detectable  $T_1$  differences while still supporting biexponential-like ADC decay curves similar to those observed experimentally. Alternative explanations for the observed nonexponential ADC decay curves of brain water in vivo which do not explicitly invoke a two-compartment model remain distinct possibilities, however, and subject to further experimental and theoretical investigations.

## APPENDIX

Karger et al. presented expressions for the signal decay with b-factor arising from a two-component system in exchange (32) intrinsically derived using the assumption that  $\delta \ll \Delta$ . The solution for the decay is biexponential in form, though the apparent diffusion coefficients  $D_1$  and  $D_2$ , and the apparent volume fractions  $A_1$  and  $A_2$ , change with b-factor. In particular, for a normalized decay in which  $A_1 + A_2 = 1$  and for which  $D_1 > D_2$  these parameters read

$$D_{1,2} = [D_f + D_g + (k_{fg} + k_{gf})/(\delta\gamma G)^2]/2 \pm \Theta \quad [A1]$$

where

$$2\Theta = \{[D_f - D_g + (k_{fg} - k_{gf})/(\delta\gamma G)^2]^2 + 4k_{fg}k_{gf}/(\delta\gamma G)^4\}^{1/2} \quad [A2]$$

and

$$A_2 = (gD_g + fD_f - D_1)/(D_2 - D_1). \quad [A3]$$

Here,  $f$  and  $g$  are the actual volume fractions of the two pools with  $f + g = 1$ ,  $k_{fg}$  and  $k_{gf}$  are the exchange rates in  $\text{sec}^{-1}$  between the two compartments. These four parameters are constrained by the steady state relationship  $fk_{fg} = gk_{gf}$ .  $D_f$  and  $D_g$  are the intrinsic diffusion coefficients within each compartment. Only in the absence of exchange will the parameters extracted experimentally from biexponential fits of signal decay with b-factor directly reflect the intrinsic volume fractions and diffusion coefficients of each compartment. In the more general case, these parameters depend on the b-factor through the gradient strength  $G$  and the timing variables  $\delta$  and  $\Delta$ .

For a two compartment system with intrinsic relaxation rates  $R_{1f}$  and  $R_{1g}$  and fractional amplitudes  $f$  and  $g$ , the apparent relaxation rates and amplitudes of the resultant biexponential  $\text{aexp}(-R_{1a}T) + \text{bexp}(-R_{1b}T)$  measured experimentally using quantities like that defined in Eq. [4] are given by the following set of relations (31):

$$R_{1a} = C_1 - C_2 \quad [A4]$$

$$R_{1b} = C_1 + C_2 \quad [A5]$$

$$C_1 = (R_{1f} + R_{1g} + k_{gf} + k_{fg})/2 \quad [A6]$$

$$C_2 = \{[R_{1f} - R_{1g} + k_{fg} - k_{gf}]^2 + 4k_{gf}k_{fg}\}^{1/2}/2 \quad [A7]$$

$$b = 1/2 - [(f - g)(R_{1g} - R_{1f}) + k_{gf} + k_{fg}]/(4C_2) \quad [A8]$$

These expressions were used to calculate the results shown in Fig. 6 utilizing  $R_{1f} = 0.5 \text{ sec}^{-1}$ ,  $R_{1g} = 1.5 \text{ sec}^{-1}$ ,  $f = 0.2$ , and  $g = 0.8$ .

## REFERENCES

1. Beauchamp NJ, Bryan RN. Acute cerebral infarction: a pathophysiological review and radiologic perspective. *AJR Am J Roentgen* 1998;171:73-84.
2. Koroshetz WJ, Gonzalez G. Diffusion-weighted MRI. An ECG for "Brain Attack." *Ann Neurol* 1997;41:565-566.
3. Lutsep HL, Albers GW, DeCrespigny A, Kamar GM, Marks MP, Moseley ME. Clinical utility of diffusion-weighted magnetic resonance imaging in the assessment of ischemic stroke. *Ann Neurol* 1997;41:574-580.
4. Hajnal JV, Doran M, Hall AS, Collins AG, Oatridge A, Pennock JM, Young IR, Bydder GM. MR imaging of anisotropically restricted diffusion of water in the nervous system: technical, anatomic, and pathologic considerations. *J Comput Assist Tomogr* 1991;15:1-18.
5. Nomura K, Sakuma H, Takeda K, Okuda Y, Nakagawa T. Diffusional anisotropy of the human brain assessed with diffusion-weighted MR: relation with normal brain development and aging. *Am J Neuroradiol* 1994;15:231-238.
6. Basser PJ, Mattiello J, LeBihan D. MR diffusion tensor spectroscopy and imaging. *Biophys J* 1994;66:259-267.
7. Pierpaoli C, Basser PJ. Toward a quantitative assessment of diffusion anisotropy. *Magn Reson Med* 1996;36:893-906.
8. Basser PJ, Pierpaoli C. A simplified method to measure the diffusion tensor from seven MR images. *Magn Reson Med* 1998;39:928-934.
9. Peled S, Gudbjartsson H, Westin C-F, Kikinis R, Jolesz FA. Magnetic resonance imaging shows orientation and asymmetry of white matter fiber tracts. *Brain Res* 1998;780:27-33.
10. Huppi PS, Maier SE, Peled S, Zientara G, Barnes PD, Jolesz FA, Volpe JJ. Microstructural development of human newborn cerebral white matter assessed in vivo by diffusion tensor magnetic resonance imaging. *Ped Res* 1998;44:584-590.

11. Niendorf T, Dijkhuizen RM, Norris DG, van Lookeren Campagne M, Nicolay K. Biexponential diffusion attenuation in various states of brain tissue: implications for diffusion-weighted imaging. *Magn Reson Med* 1996;36:847-857.
12. Mulkern RV, Gudbjartsson H, Westin C-F, Zengingonul HP, Gartner W, Guttman CRG, Robertson R, Kyriakos W, Schwartz R, Holtzman D, Jolesz FA, Maier SE. Multi-component apparent diffusion coefficients in human brain. *NMR in Biomed* 1999;12:51-62.
13. Zengingonul HP, Mulkern RV. Measurement and analysis of nonexponential signal decay curves in brain diffusion and muscle relaxation magnetic resonance studies in humans. *Int J Imaging Syst Technol* 1999;10:294-303.
14. Le Bihan D, Moonen CTW, van Zijl PCM, Pekar J, Despres D. Measuring random microscopic motion of water in tissues with MR imaging: a cat brain study. *J Comput Assist Tomogr* 1991;15:19-25.
15. Conturo TE, McKinstry RC, Aronovitz JA, Neil JJ. Diffusion MRI. Precision, accuracy and flow effects. *NMR Biomed* 1995;8:307-332.
16. Snedecor GW, Cochran WC. *Statistical methods*, 7th ed. Ames, IA: Iowa State University Press; 1980.
17. Mudholkar GS, McDermott M, Srivastava DK. A test of p-variate normality. *Biometrika* 1992;79:850-854.
18. Mathsoft, S-PLUS 4 Guide to statistics. Data Analysis Products Division. Seattle: Mathsoft, 1997.
19. Koenig SH, Brown RD III, Spiller M, Lundbom N. Relaxometry of brain: why white matter appears bright in MRI. *Magn Reson Med* 1990;14:482-495.
20. Yamada I, Aung W, Himeno Y, Nakagawa T, Shibuya H. Diffusion coefficients in abdominal organs and hepatic lesions: evaluation with intravoxel incoherent motion echo-planar MR imaging. *Radiology* 1999;210:617-623.
21. Li JG, Stanisz GJ, Henkelman RM. Integrated analysis of diffusion and relaxation of water in blood. *Magn Reson Med* 1998;40:79-88.
22. Stanisz GJ, Li JG, Wright GA, Henkelman RM. Water dynamics in human blood via combined measurements of  $T_2$  relaxation and diffusion in the presence of gadolinium. *Magn Reson Med* 1998;39:223-233.
23. van Zijl PCM, Moonen CTW, Faustino P, Pekar J, Kaplan O, Cohen JS. Complete separation of intracellular and extracellular information in NMR spectra of perfused cells by diffusion-weighted spectroscopy. *Proc Natl Acad Sci* 1991;88:3228-3232.
24. Pilatus U, Shim H, Artemov D, Davis D, van Zijl PCM, Glickson JD. Intracellular volume and apparent diffusion constants of perfused cancer cell cultures, as measured by NMR. *Magn Reson Med* 1997;37:825-832.
25. Pfeuffer J, Flogel U, Leibfritz D. Monitoring of cell volume and water exchange time in perfused cells by diffusion-weighted  $^1\text{H}$  NMR spectroscopy. *NMR Biomed* 1998;11:11-18.
26. Pfeuffer J, Flogel U, Dreher W, Leibfritz D. Restricted diffusion and exchange of intracellular water: theoretical modelling and diffusion time dependence of  $^1\text{H}$  NMR measurements on perfused glial cells. *NMR Biomed* 1998;11:19-31.
27. Stanisz GJ, Zafer A, Wright GA, Henkelman RM. An analytical model of restricted diffusion in bovine optic nerve. *Magn Reson Med* 1997;37:103-111.
28. Stanisz GJ, Henkelman RM. Diffusional anisotropy of  $T_2$  components in bovine optic nerve. *Magn Reson Med* 1998;40:405-410.
29. van Gelderen P, de Vleeschouwer MHM, Despres D, Pekar J, van Zijl PCM, Moonen CTW. Water diffusion and acute stroke. *Magn Reson Med* 1994;31:154-163.
30. Buckley DL, Bui JD, Phillips MI, Zelles T, Inglis BA, Plant HD, Blackband SJ. The effect of ouabain on water diffusion in the rat hippocampal slice measured by high resolution NMR imaging. *Magn Reson Med* 1999;41:137-142.
31. Zimmerman JR, Brittin WE. Nuclear magnetic resonance studies in multiple phase systems: lifetime of a water molecule in an adsorbing phase on silica gel. *J Phys Chem* 1957;61:1328-1333.
32. Karger J, Pfeifer H, Heink W. Principles and applications of self-diffusion measurements by NMR. *Adv Magn Reson* 1988;12:1-89.
33. Assaf T, Cohen Y. In vivo and in vitro bi-exponential diffusion of N-acetyl aspartate (NAA) in rat brain: a potential structural probe? *NMR in Biomed* 1998;11:67-74.
34. Helmer KG, Dardzinski BJ, Sotak CH. The application of porous-media theory to the investigation of time-dependent diffusion in in vivo systems. *NMR in Biomed* 1995;8:297-306.
35. Mitra PP, Sen PN, Schwartz LM, Le Doussal P. Diffusion propagator as a probe of the structure of porous media. *Phys Rev Lett* 1992;68:3555-3558.
36. Latour LL, Mitra PP, Kleinberg RL, Sotak CH. Time-dependent diffusion coefficient of fluids in porous media as a probe of surface-to-volume ratio. *J Magn Reson Series A* 1993;101:342-346.
37. Peled S, Cory CG, Raymond SA, Kirschner DA, Jolesz FA. Water diffusion,  $T_2$ , and compartmentation in frog sciatic nerve. *Magn Reson Med* 1999;42:911-918.
38. Mulkern RV, Wong STS, Jakab P, Bleier AR, Sandor T, Jolesz FA. CPMG imaging sequences for high field in vivo transverse relaxation studies. *Magn Reson Med* 1990;16:67-79.
39. Ernst T, Kreis R, Ross BD. Absolute quantitation of water and metabolites in the human brain. I. Compartments and water. *J Magn Reson Series B* 1993;102:1-8.
40. MacKay AL, Whittall KP, Adler J, Li DKB, Paty DW, Graeb D. In vivo visualization of myelin water in brain by magnetic resonance. *Magn Reson Med* 1994;31:673-677.

**Publication:**

Paper III:

Sensitivity Profiles from an Array of Coils for Encoding and Reconstruction In Parallel (SPACE RIP).

Authors:

**Walid E. Kyriakos**, Lawrence P. Panych, Daniel F. Kacher, Carl-Frerick Westin, Sumi M. Bao, Robert V. Mulkern, and Ferenc A. Jolesz.

Journal:

Magnetic Resonance in Medicine (MRM)  
44: 301 – 308, 2000.

# Sensitivity Profiles From an Array of Coils for Encoding and Reconstruction in Parallel (SPACE RIP)

Walid E. Kyriakos,<sup>1,2\*</sup> Lawrence P. Panych,<sup>1</sup> Daniel F. Kacher,<sup>1</sup> Carl-Fredrick Westin,<sup>1</sup> Sumi M. Bao,<sup>1</sup> Robert V. Mulkern,<sup>1,2</sup> and Ferenc A. Jolesz<sup>1</sup>

A new parallel imaging technique was implemented which can result in reduced image acquisition times in MRI. MR data is acquired in parallel using an array of receiver coils and then reconstructed simultaneously with multiple processors. The method requires the initial estimation of the 2D sensitivity profile of each coil used in the receiver array. These sensitivity profiles are then used to partially encode the images of interest. A fraction of the total number of  $k$ -space lines is consequently acquired and used in a parallel reconstruction scheme, allowing for a substantial reduction in scanning and display times. This technique is in the family of parallel acquisition schemes such as simultaneous acquisition of spatial harmonics (SMASH) and sensitivity encoding (SENSE). It extends the use of the SMASH method to allow the placement of the receiver coil array around the object of interest, enabling imaging of any plane within the volume of interest. In addition, this technique permits the arbitrary choice of the set of  $k$ -space lines used in the reconstruction and lends itself to parallel reconstruction, hence allowing for real-time rendering. Simulated results with a 16-fold increase in temporal resolution are shown, as are experimental results with a 4-fold increase in temporal resolution. *Magn Reson Med* 44:301–308, 2000. © 2000 Wiley-Liss, Inc.

**Key words:**  $k$ -space sampling; parallel imaging; sensitivity profiles; parallel reconstruction

Despite the many advances in ultrafast MRI, there is always a need for further increases in the speed of image acquisition. Dynamic imaging applications like cardiac and interventional imaging would be greatly served with an order of magnitude reduction in scan time without sacrificing spatial resolution and signal to noise ratio (SNR). Conventional multiecho imaging techniques such as RARE and EPI (1,2) are currently very fast. The new field of parallel imaging can be combined with these methods to further increase imaging speed.

In previous work on parallel imaging, Hutchinson and Raff (3) demonstrated the theoretical feasibility of fast data acquisitions using multiple detectors in MRI. In a subsequent work, Kwiat et al. (4) investigated methods to solve the inverse source problem on MR signals received in multiple RF receiver coils. Their technique required the use of a number of RF coils equal to the number of pixels in the image, as well as greatly increased receiver coil sensitivities. These requirements are quite impractical in conventional MR imaging, where the usual number of

pixels in an image is on the order of  $256 \times 256$ , hence the technique was never successfully used in medical imaging.

A number of more promising parallel imaging techniques have been described in the literature (5–7) which use the sensitivity profiles of RF receiver coils for spatial encoding. Ra and Rim (5) described a method that uses sets of equally spaced  $k$ -space lines from multiple receiver coils and combines them with sensitivity profile information in order to remove the aliasing that occurs due to the undersampling. A 4-fold decrease in the image acquisition time of a water phantom was shown using an array of four coils, although no biological images were shown.

The SMASH method proposed by Sodickson and Manning (6) has proven more practical, yielding good results in volunteers with clinical implementations. SMASH is designed to enhance imaging speed by using multiple receiver RF coils. It is based on the computation of the sensitivity profiles of the coils in one direction. These profiles are then weighted appropriately and combined linearly in order to form sinusoidal harmonics which are used to generate the  $k$ -space lines that are missing due to undersampling. This technique showed an 8-fold increase in imaging speed. SMASH has some inflexibility in the choice of imaging planes due its restriction on the placement of receiver coils along one direction.

The SENSE method proposed by Pruessmann et al. (7) is another parallel imaging technique which relies on the use of 2D sensitivity profile information in order to reduce image acquisition times in MRI. Like SMASH, the cartesian version of SENSE requires the acquisition of equally spaced  $k$ -space lines in order to reconstruct sensitivity weighted, aliased versions of the image. The aliasing is then removed with the use of the sensitivity profile information at each pixel. This is done by resolving in the space domain the linear system of equations obeyed by the intensity of each pixel in the image.

A generalization of SENSE was introduced by Pruessmann et al. (8) which would allow for data to be sampled along arbitrary  $k$ -space trajectories. A high computational cost, however, accompanies the arbitrary  $k$ -space sampling in generalized SENSE methods, currently making reconstruction inconvenient. An elaborate description of the differences between SMASH and SENSE can be found in the SENSE manuscript (7).

In this article, we present a parallel imaging and reconstruction technique which attempts to generalize the SMASH approach by allowing for the arbitrary placement of RF receiver coils around the object to be imaged as well as for the use of any combination of  $k$ -space lines as opposed to regularly spaced ones. In addition, our reconstruction technique is completely parallel, allowing for

<sup>1</sup>Department of Radiology, Brigham and Women's Hospital, Boston, Massachusetts.

<sup>2</sup>Department of Radiology, Children's Hospital, Boston, Massachusetts.

A preliminary account of this work was presented at the 8th Annual Meeting of the ISMRM, Denver, CO, 2000 (Abstract 1506).

\*Correspondence to: Walid E. Kyriakos, Department of Radiology, Brigham and Women's Hospital, 221 Longwood Avenue, Boston, MA 02115.

Received 12 July 1999; revised 27 March 2000; accepted 30 March 2000.

© 2000 Wiley-Liss, Inc.

real-time rendering possibilities with the use of multiple processors.

## METHODS

### Encoding Scheme

The concept of parallel imaging is based on using multiple receiver coils, with each providing independent information about the image.

The MR signal received in a coil having  $W_k(x, y)$  as its complex 2D sensitivity profile, when neglecting all relaxation phenomena, can be written as:

$$s_k(G_y^g, t) = \iint r(x, y)W_k(x, y)e^{i\gamma(G_x x t + G_y^g y \tau)} dx dy, \quad [1]$$

where  $r(x, y)$  denotes the proton density function,  $G_x$  represents the readout gradient amplitude applied in the  $x$  direction,  $G_y^g$  represents the phase encoding gradient applied during the  $g^{th}$  acquisition,  $x$  and  $y$  represent the  $x$  and  $y$  positions, respectively, and  $\tau$  is the pulse width of the phase encoding gradient  $G_y^g$ .

In most conventional serial imaging sequences, the readout gradient is constant along one direction and the phase encoding is applied along an orthogonal direction. In addition, only one receiver coil is used to collect all the data required to reconstruct a digitized version of  $r(x, y)$ , with the tacit assumption that  $W_k(x, y) = 1$ . To achieve this, the phase encoding gradient  $G_y$  is varied so as to cover all of  $k$ -space with the desired resolution. For each value of  $G_y^g$ , an echo is acquired, making serial imaging a time-consuming procedure. In this technique, we use sensitivity profile information from a number of receiver coils in order to minimize the number of acquisitions needed to estimate and reconstruct  $r(x, y)$ . Taking the Fourier transform of Eq. [1] along the  $x$  direction when a phase encoding gradient  $G_y^g$  has been applied yields:

$$S_k(G_y^g, x) = \int r(x, y)W_k(x, y)e^{i\gamma(G_y^g y \tau)} dy, \quad [2]$$

which is the phase modulated projection of the sensitivity weighted image onto the  $x$  axis. For the purpose of dis-

cretization, we expand  $r(x, y)$  and  $W_k(x, y)$  along the  $y$  direction in terms of a spatially localized set of orthogonal sampling functions  $\Omega_n(y)$  to obtain the following equations:

$$r(x, y) = \sum_{n=1}^N \rho(x, n)\Omega_n(y), \quad [3]$$

and,

$$W_k(x, y)e^{i\gamma(G_y^g y \tau)} = \sum_{n'=1}^N W_k(x, n')e^{i\gamma(G_y^g n' \tau)}\Omega_{n'}(y). \quad [4]$$

where  $N$  is the number of pixels in the  $y$  direction. Combining Eqs. [3] and [4], we get:

$$S_k(G_y^g, x) = \int \sum_{n=1}^N \rho(x, n)\Omega_n(y) \sum_{n'=1}^N W_k(x, n')e^{i\gamma(G_y^g n' \tau)}\Omega_{n'}(y) dy. \quad [5]$$

Rearranging the terms for simplification yields:

$$S_k(G_y^g, x) = \sum_{n=1}^N \rho(x, n)W_k(x, n')e^{i\gamma(G_y^g n' \tau)} \int \Omega_n(y)\Omega_{n'}(y) dy. \quad [6]$$

Since  $\Omega(y)$  is orthonormal, we have:

$$\int \Omega_n(y)\Omega_{n'}(y) dy = \delta(n, n'). \quad [7]$$

Therefore, Eq. [6] can be written as:

$$S_k(G_y^g, x) = \sum_{n=1}^N \rho(x, n)W_k(x, n)e^{i\gamma(G_y^g n \tau)}. \quad [8]$$

This expression can be converted to matrix form for each position  $x$  along the horizontal direction of the image, as follows:

$$\begin{pmatrix} S_1(G_y^1, x) \\ \vdots \\ S_1(G_y^F, x) \\ S_2(G_y^1, x) \\ \vdots \\ S_2(G_y^F, x) \\ \vdots \\ S_k(G_y^1, x) \\ \vdots \\ S_k(G_y^F, x) \end{pmatrix} = \begin{pmatrix} W_1(x, 1)e^{i\gamma(G_y^1 \tau)} & \cdots & W_1(x, N)e^{i\gamma(G_y^1 N \tau)} \\ \vdots & \cdots & \vdots \\ W_1(x, 1)e^{i\gamma(G_y^F \tau)} & \cdots & W_1(x, N)e^{i\gamma(G_y^F N \tau)} \\ W_2(x, 1)e^{i\gamma(G_y^1 \tau)} & \cdots & W_2(x, N)e^{i\gamma(G_y^1 N \tau)} \\ \vdots & \cdots & \vdots \\ W_2(x, 1)e^{i\gamma(G_y^F \tau)} & \cdots & W_2(x, N)e^{i\gamma(G_y^F N \tau)} \\ \vdots & \cdots & \vdots \\ W_k(x, 1)e^{i\gamma(G_y^1 \tau)} & \cdots & W_k(x, N)e^{i\gamma(G_y^1 N \tau)} \\ \vdots & \cdots & \vdots \\ W_k(x, 1)e^{i\gamma(G_y^F \tau)} & \cdots & W_k(x, N)e^{i\gamma(G_y^F N \tau)} \end{pmatrix} \cdot \begin{pmatrix} \rho(x, 1) \\ \rho(x, 2) \\ \rho(x, 3) \\ \vdots \\ \vdots \\ \vdots \\ \rho(x, N) \end{pmatrix} \quad [9]$$

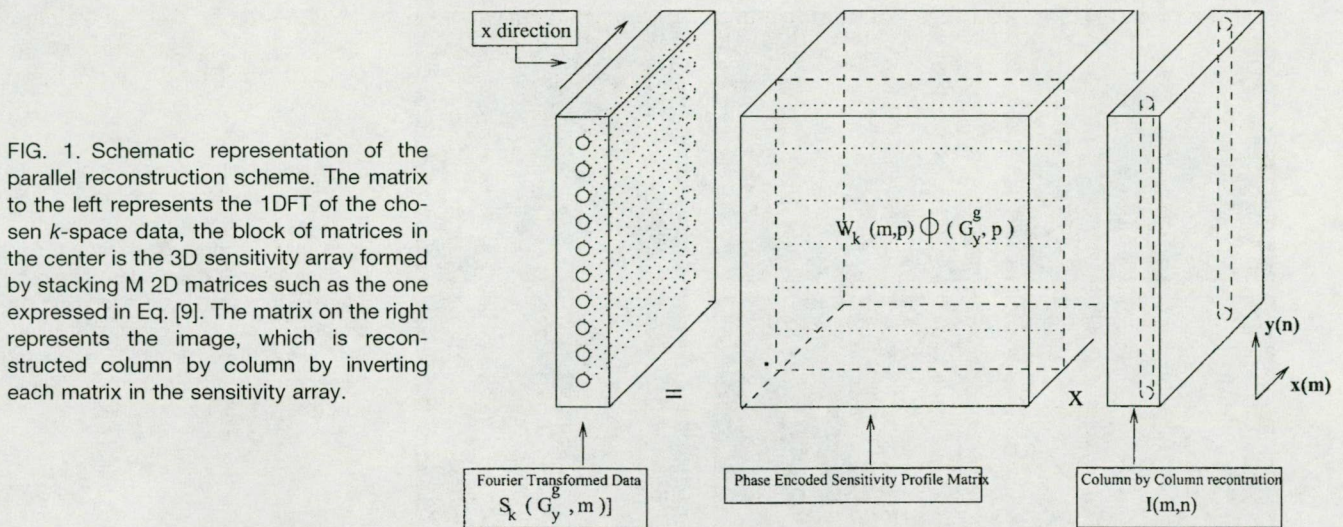


FIG. 1. Schematic representation of the parallel reconstruction scheme. The matrix to the left represents the 1DFT of the chosen  $k$ -space data, the block of matrices in the center is the 3D sensitivity array formed by stacking  $M$  2D matrices such as the one expressed in Eq. [9]. The matrix on the right represents the image, which is reconstructed column by column by inverting each matrix in the sensitivity array.

where  $F$  is the number of phase encodes used in the experiment, and  $K$  is the number of coils.

Equation [9] is a matrix equation where the term on the left side of the equality is a  $K \times F$  element vector containing the  $F$  phase encoded values for all  $K$  coils. The term on the far right is an  $N$ -element vector representing the “image” for one column. The middle term in Eq. [9] is a matrix with  $K \times F$  rows and  $N$  columns which is constructed based on the sensitivity profiles and phase encodes used. Hence, this approach is not restricted to the case where  $K \times F = N$ . Solving Eq. [9] for each position along the  $x$  axis yields a column by column reconstruction of the image.

Figure 1 shows a schematic representation of the reconstruction process. As described above, each column in the image is reconstructed separately. In the case where the image matrix has  $N$  rows and  $M$  columns, a block of  $M$  matrices must be inverted to reconstruct the  $M$  columns of the image. The matrices are not necessarily square, so that a pseudoinverse must be computed for each column. The choice of the number of phase encodes  $F$  affects the quality of the reconstruction. Increasing  $F$  results in an increase of the rank of the matrices, yielding pseudoinverses that are better conditioned. There is a large computation load associated with this reconstruction; however, the potential for parallelization is obvious, since each column can be reconstructed separately. For each slice, the pseudoinverses have to be computed only once. Subsequent updates of the same slice can be reconstructed by simple matrix vector multiplication, reducing reconstruction times to real-time rates.

#### Conditioning and the Choice of the Phase Modulations

The reconstruction scheme outlined in the previous section is based on matrix inversion. In order to ensure a stable and robust reconstruction, the condition number of the inverted matrices, defined as the ratio of the largest eigenvalue to the lowest eigenvalue, should be minimized (9). Equation [9] shows that the condition number depends on the number of phase encodes  $F$  acquired per coil. It is also affected by the choice of the phase encodes used in

the acquisition, as well as on the specifications of the receiver coils, which include the sensitivity profiles and the RF penetration. In addition, the condition number is affected by the SNR of the sensitivity profile estimations.

Our results show (Fig. 6) that increasing the number of phase encodes used in the reconstruction would enhance the conditioning of the reconstruction matrices. To avoid errors due to numerical propagation, the pseudoinverse of each reconstruction matrix is computed after setting a minimum threshold to the eigenvalues. This effectively removes any noise amplification due to bad conditioning. For our reconstructions, we chose a cutoff threshold of 5% of the maximum eigenvalue whereby all eigenvalues below that threshold are set to zero and therefore do not contribute to the reconstruction. Our results also show that more RF penetration contributes to better conditioning. Finally, if both the choice of the  $k$ -space encodes and the coil penetration are set, the condition number would be expected to depend on the  $k$ -space characteristic of the sensitivity profiles of the receiver coils.

#### $k$ -Space Coverage

In order to appropriately cover the  $k$ -space of the image  $I(x, y)$ , the choice of the phase modulations used in the inversion matrix should be determined by the frequency content of the sensitivity profile. In the spatial domain, the image received in a coil having a sensitivity profile  $W_c(x, y)$  can be written as  $I_c(x, y) = I(x, y)W_c(x, y)$ . In the frequency domain, the  $k$ -space profile of  $I_c(x, y)$  is the convolution of the  $k$ -space profile  $I(k_x, k_y)$  of the image  $I(x, y)$ , with the  $k$ -space profile  $W_c(k_x, k_y)$  of the sensitivity profile  $W_c(x, y)$ . This convolution amounts to a blurring of the  $k$ -space data  $I(k_x, k_y)$  of the image. Since a different convolution is performed for each coil, a different blurring of  $I(k_x, k_y)$  occurs at each coil. Subsampling the convolved  $k$ -space data received in different coils therefore results in different coverages of the  $k$ -space of the image  $I(x, y)$ . Hence, in order to get the best  $k$ -space coverage of the  $I(x, y)$  for a given  $W_c(x, y)$ , it is necessary to optimally sample the  $k$ -space data from all the coils.

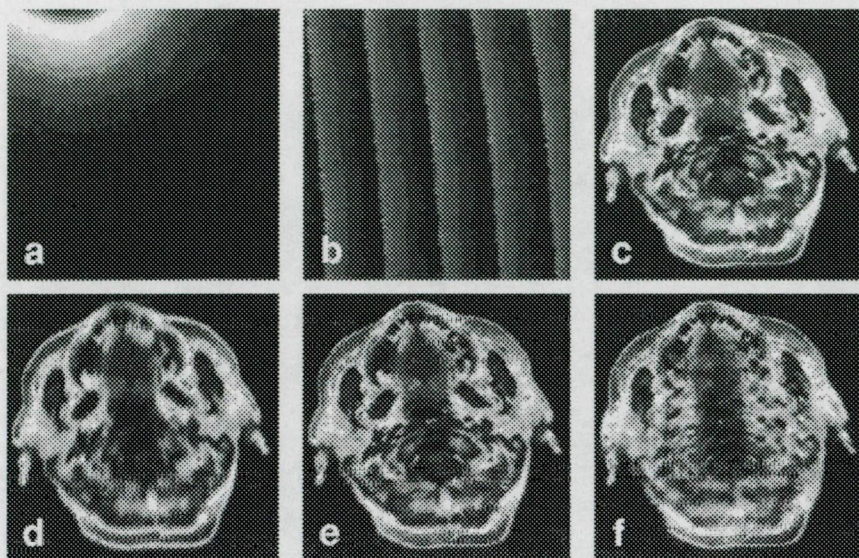


FIG. 2. **a:** Magnitude of one of the sensitivity profiles used for encoding. **b:** Phase profile used on all sensitivity profiles. **c:** Reference image reconstructed by 2DFT using all  $k$ -space lines. Sixteen lines of  $k$ -space were used in the simulation assuming 16 coils arranged every  $22.5^\circ$  around the head. Parts **d–f** were reconstructed by using the  $k$ -space lines acquired from skipping, respectively, 1, 8, and 16 lines.

In contrast to SMASH (6), which requires the use of equally spaced  $k$ -space lines, this technique is completely flexible as to that choice. In this work, we use equally spaced  $k$ -space lines to demonstrate the technique, and show how more optimal sets of  $k$ -space lines can be found to achieve better results. Finding the optimal set of  $k$ -space lines is, however, a subject beyond the scope of the current work.

#### Sensitivity Profile Calculation

Our method is based on using the sensitivity profiles of RF pickup coils in order to encode MR images. To calculate these profiles, a number of techniques described in the literature could be used (7,10–12). In this article, we use a technique that only requires comparison between body coil and surface coil images without any filtering or other numerical manipulations. It was chosen for its simplicity and adaptability to real-time applications. A baseline image of a homogeneous water phantom is acquired using an RF coil with a homogeneous sensitivity profile covering the whole image. This image can be written as  $I(x, y)$ . Subsequently, individual images of the same water phantom are acquired using each of the surface coils. The image acquired using the  $k^{\text{th}}$  coil can be represented as  $I(x, y)W_k(x, y)$  where  $W_k(x, y)$  is the sensitivity profile of the surface coil. Taking the point-by-point ratio of the two images yields the sensitivity profile  $W_k(x, y)$ .

The sensitivity profiles of the receiver coils depend on the loading. We assume that the variation incurred by these profiles amounts to a constant scaling between any two different loads. Therefore, in order to find the sensitivity profile of the receiver coils when loaded with an arbitrary body of interest, we perform a sensitivity profile estimation on that body as described above, then compare it to the sensitivity profiles computed on the homogeneous water phantom in order to extract the scaling factor. The sensitivity profiles calculated from the homogeneous water phantom are then multiplied by the scaling factor and used in the encoding scheme. This is done in order to get maximum coverage of the field of view by the sensitivity

profiles. Optimizations of the computed sensitivity profiles by smoothing and interpolation have been proposed in SENSE (7) and may well be used to refine the sensitivity profile estimations in our technique, leading to better conditioned reconstructions.

## RESULTS

We show the results from a simulation of the method assuming a 16-element coil as well as the results from an experimental implementation of the method with a 4-element array coil. All experiments were performed on 1.5 T GE clinical MRI systems operating at either the 5.7 SIGNA or 8.2.5 LX hardware-software configurations.

### Simulation Results

#### Noise-Free, Low-Frequency Profiles

In order to assess the feasibility of the technique under ideal conditions, simulations were performed. We acquired a homogeneous image of a brain, with a matrix size of  $256 \times 256$ , using a head coil, then computed an ideal, noise-free sensitivity profile having a  $1/r^2$  falloff and a linear phase profile. Its magnitude image is shown in Fig. 2a, and its phase profile is shown in Fig. 2b. Then, 16 rotated magnitude sensitivity profiles were computed with an angle of  $2\pi/16$  between any adjacent two of them and given the same phase profile shown in Fig. 2b. Next, the computed sensitivity profiles were multiplied point by point with the brain magnitude image in order to get approximations of sensitivity weighted images from surface coils placed at different positions. The sensitivity-weighted images are then Fourier-transformed in two dimensions in order to get the  $k$ -space data. Subsequently, 16 lines of  $k$ -space data were taken from each matrix and used to reconstruct the head image. Image matrix size was chosen to be  $256 \times 256$ .

As mentioned in the previous section, the choice of the  $k$ -space lines affects the image resolution. In Fig. 2d,e,f, we show three images reconstructed using different sets of

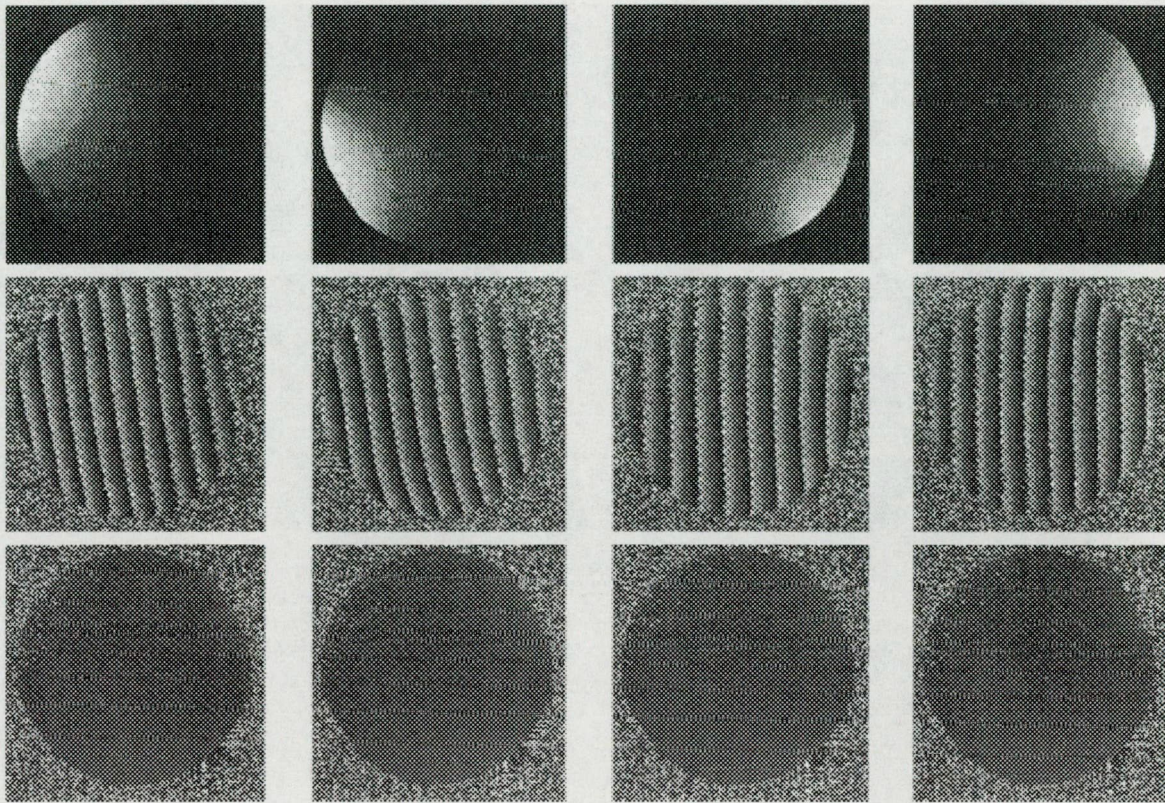


FIG. 3. Experiment results. The top row shows the magnitude images of the 2D sensitivity profiles as computed from a homogeneous water phantom from all four coils in the phased array. The middle row shows the phase images of the sensitivity profiles. The bottom row shows the adjusted phase profiles after linear shifting.

$k$ -space data in the  $K \times F = N$  case. These computations required the inversion of 256 matrices each of size  $256 \times 256$  and were completed in less than 600 sec on a SUN UltraSparc machine with a processor speed of 266 MHz. These reconstructions can be performed in less than 1 sec if a processor is used for each column and with current processor speeds of over 700 MHz. This represents a clear advantage over the generalized SENSE reconstruction method, especially when the choice of the imaged slice is dynamically changed and a complete calculation of the pseudoinverses is needed. Reconstruction speed increases beyond real-time rates, however, when the same slice is being refreshed, and the calculation is reduced to a set of vector matrix multiplications.

Figure 2c shows the reference image reconstructed using a 2DFT on all  $k$ -space lines. Figure 2d shows a reconstruction using the 16 lines of  $k$ -space going between  $k = -7$  and  $k = 8$ ; Fig. 2e shows a reconstruction using the lines of  $k$ -space going between  $k = -79$  to  $k = 80$  and skipping 8 lines; finally, Fig. 2f shows a reconstruction using the 16 lines of  $k$ -space going between  $k = -127$  to  $k = 128$  and skipping 16 lines. It can be seen that Fig. 2e represents the best result of the three, as it shows better resolution than Fig. 2d and no artifact as in Fig. 2f. A certain deterioration of the image is observed in Fig. 2f as 16 lines are skipped before reconstruction. This suggests that the  $k$ -space coverage from such a subsampling is not appropriate.

### Experimental Results

Two imaging experiments were done in order to test the performance of the technique in practical situations.

#### *Imaging With the Cardiac Coil*

In the first experiment we imaged a human head using a phased array cardiac coil with 4 elements of size  $10 \times 10$  cm fixed around the FOV. Image matrix size was chosen to be  $128 \times 128$ . First, a baseline FSE  $T_2$ -weighted image was acquired from a homogeneous water phantom using the body coil with TR = 2 s, TE = 102 ms, and ETL = 12. The phased array coil was then used to simultaneously collect four images, one from each coil. These images were used in conjunction with the baseline image to calculate the sensitivity profiles of the coils at different positions using the point-by-point ratio method as described above. The magnitude images of the sensitivity profiles are shown in Fig. 3 (top) and their respective phase images are shown below them in Fig. 3 (middle). Initial calibration was performed in order to remove a linear phase shift which exists between the different coils. This calibration is necessary to insure that the  $k$ -space data in all coils is identically centered and that no destructive interference would arise during reconstruction. This finding is common to all parallel imaging techniques (6,7) where phase fidelity is crucial for the stability of the reconstructions. The resulting phase images of the adjusted profiles are shown in Fig. 3 (bottom).

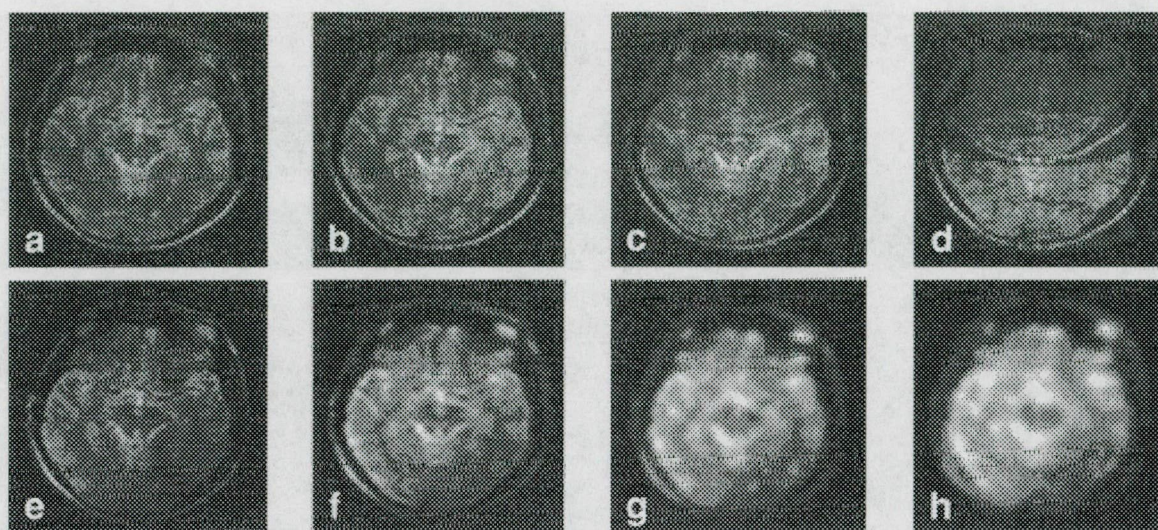


FIG. 4. Experiment results. The parts on the top show the reconstruction using our technique with the cardiac coil array, and choosing equally spaced  $k$ -space lines. The number of  $k$ -space lines used are, from left to right, respectively: 128, 64, 43, and 32. The parts shown on the bottom represent the images obtained by summing the magnitude of the images reconstructed using the middle lines of  $k$ -space in all four coils. The number of  $k$ -space lines used from left to right are equal to those of the corresponding top parts.

The calibrated profiles were subsequently used to encode a brain image as described previously. In a first reconstruction, we show in the top half of Fig. 4 the results of this technique, where equally spaced  $k$ -space lines were used. Figure 4a shows an image reconstructed using all 128  $k$ -space lines. Figure 4b was reconstructed using 64 equally spaced and centered  $k$ -space lines; Fig. 4c was reconstructed using 43  $k$ -space lines and Fig. 4d was reconstructed using 32  $k$ -space lines. Each of these images is shown on top of an image reconstructed by using the same number of  $k$ -space lines in the keyhole mode (13). These images are shown, respectively, in Fig. 4e–h.

In a second reconstruction, we show the effect of choosing different sets of lines of  $k$ -space to enhance the rendering.

These results are shown in Fig. 5 where different sets of 32 lines of  $k$ -space are used to reconstruct a brain image. Below each image, we show the lines of  $k$ -space that were used to reconstruct it with our technique. The leftmost image is obtained by using 32 equally spaced lines in  $k$ -space whereby the consecutive images are reconstructed by using variations of denser coverages of the center of  $k$ -space. Reconstructions were performed on a Sun Ultrasparc station having a processor speed of 266 MHz. In all cases, reconstruction times were less than 160 sec.

#### *Imaging With the Torso Coil*

In order to test the effect of coil penetration on the reconstruction in practical situations, we repeated the previous

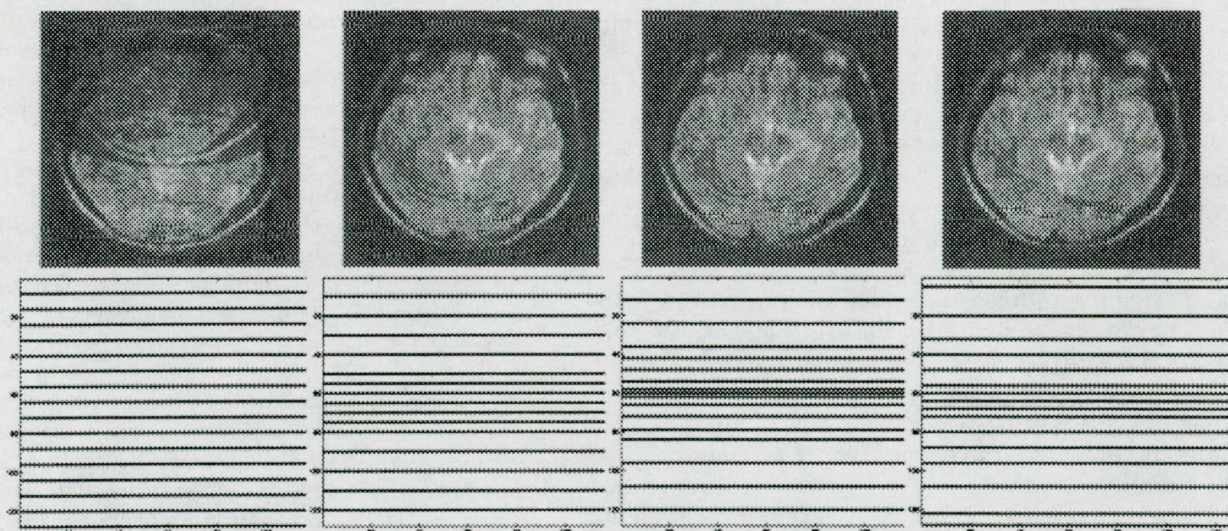


FIG. 5. Experiment results. The parts on the top show the reconstruction using different sets of 32 lines of  $k$ -space with our technique using the cardiac coil array. Below each part we show the corresponding  $k$ -space lines chosen.

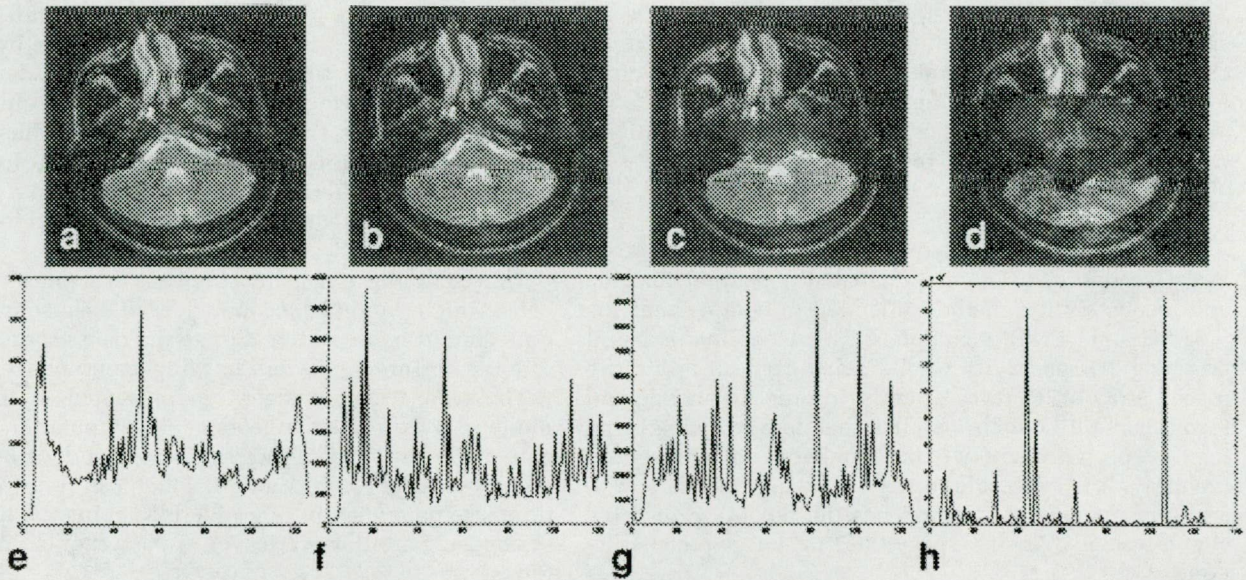


FIG. 6. Experiment results. The parts on the top show the reconstruction using our technique with the torso coil array and choosing equally spaced  $k$ -space lines. The number of  $k$ -space lines used are, from left to right, respectively: 128, 64, 43, and 32. The parts shown on the bottom represent the plot of the condition numbers of the reconstruction matrix for each column. The number of  $k$ -space lines used from left to right are equal to those of the corresponding top parts.

experiment (FSE, TR = 2 s, TE = 102 ms, ETL = 12) using the phased array torso coil with four elements of size (15 × 15 cm) fixed around the FOV. Image matrix size was chosen to be 128 × 128.

In a first reconstruction, we show in the top half of Fig. 6 the results of this technique, by using equally spaced  $k$ -space lines. Figure 6a shows an image reconstructed using all 128  $k$ -space lines, Fig. 6b was reconstructed by using 64  $k$ -space lines, Fig. 6c was reconstructed using 43  $k$ -space lines, and Fig. 6d was reconstructed using 32  $k$ -space lines. Each of these images is shown on top of a plot showing the magnitude of the condition number of the reconstruction matrix for every column in the image. It

can be seen that the condition number increases when fewer  $k$ -space lines are used, hence a slight overdetermination ( $K \times F > N$ ) is recommended for better reconstructions. We also note that the reconstruction shown in Fig. 6c contains less artifact than Fig. 4c due to the larger coil elements.

In a second reconstruction, we show the effect of choosing different sets of lines of  $k$ -space to enhance the rendering. These results are shown in Fig. 7, where different sets of 32 lines of  $k$ -space are used to reconstruct a brain image. Below each image, we show the lines of  $k$ -space that were used to reconstruct it with our technique. The leftmost image is obtained by using 32 equally spaced

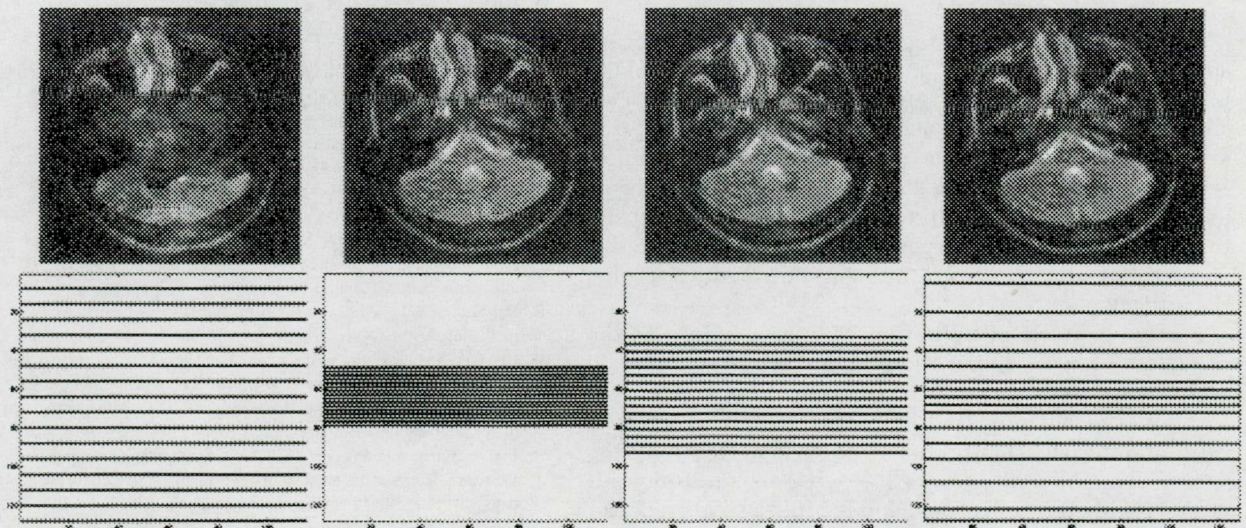


FIG. 7. Experiment results. The parts on the top show the reconstruction using different sets of 32 lines of  $k$ -space with our technique for the torso coil array. Below each part we show the corresponding  $k$ -space lines chosen.

lines in  $k$ -space whereby the consecutive images are reconstructed by using variations of denser coverages of the center of  $k$ -space. An overall improvement in image quality is seen compared to the images in Fig. 5, which we attribute to the greater penetration depth of the sensitivity profiles due to the larger coil elements.

## DISCUSSION

We have designed and implemented a parallel imaging and reconstruction method intended to complement the SMASH and SENSE techniques. This technique is based on using 2D sensitivity profile maps from an arbitrarily placed array of RF receiver coils, in order to encode and reconstruct MRI data in parallel, therefore reducing imaging time proportionately to the number of coils present in the array. It is adaptable to any imaging sequence and to arbitrary imaging planes and has the flexibility of being able to use any set of  $k$ -space lines for image reconstruction.

The placement of the RF pickup coils can be arbitrary, around the imaged field of view. This allows for the placement of more RF coils than certain parallel imaging techniques such as SMASH (6). Having more coils in the receiver array would enable faster imaging.

A clear reduction of imaging speed could be achieved using this technique. In this article, we show the simulated results of a 16-fold speed increase and experimental results with a 4-fold speed increase. Since there is a tradeoff between coil size and penetration, an optimal number of coils can be determined to yield the best results.

The reconstruction in this method is based on a matrix inversion algorithm. In order to ensure a good reconstruction, our results show that it is necessary to minimize the condition number of the inverted matrices. Better conditioning of the reconstruction matrices can be achieved with the use of more  $k$ -space data from each coil ( $K \times F > N$ ), as shown in Fig. 6e–h. Once the receiver coil and the number  $F$  of acquired  $k$ -space lines are chosen, conditioning is achieved by setting a threshold to the eigenvalues in the reconstruction matrix. This is done to minimize numerical propagation errors.

For a given number  $F$  of  $k$ -space lines used in the reconstruction, our results (Figs. 5, 7) show that the choice of the phase encodes is crucial to ensure that image resolution is similar to images acquired using full  $k$ -space data, and that artefacts due to the regular and insufficient sampling of  $k$ -space are eliminated. For all the images shown in Figs. 5 and 7, we found the condition numbers of the reconstruction matrices to be similar; however, the choice of a different set of  $k$ -space lines results in dramatically reducing the artifacts.

A current practical limitation of this technique is the need for a large number of receivers. Most commercial scanners are limited to four receivers, and the high cost of additional receivers makes having as many as 16 practically prohibitive. This problem could be solved with the use of channel multiplexers (5), whereby multiple coil outputs could be multiplexed and fed into a single receiver and later demultiplexed to get the output of each coil.

Our technique is based on the use of coil sensitivity profiles to encode spatial dimensions; therefore, a good

estimation of these profiles is crucial to ensure good results. In this article, we applied our technique by considering that the sensitivity profiles are independent of the coil loading, allowing us to extrapolate the results of the sensitivity profiles computed from a water phantom to encode other images. In reality, however, loading affects the sensitivity profiles of the coil elements and a dynamic method of profile computation would be useful to account for the different objects imaged.

This technique is sensitive to phase differences between coils, which should be accounted for in the reconstruction. Care should be taken to calibrate the data acquisition before the beginning of every imaging experiment.

The reconstruction algorithm presented in this technique allows for the independent computation of each column in the image. This technique lends itself, therefore, to parallel reconstruction, which can result in realistic image computation times while keeping the flexibility of choosing arbitrary cartesian  $k$ -space acquisition trajectories.

We believe that the limitations mentioned are surmountable, and the technique has great potential to overcome the problem of relatively long acquisition times in MRI. The parallel reconstruction algorithm should allow for real-time acquisition as well as reconstruction of MR data and may be very well suited for applications such as cardiac, functional, and interventional imaging.

## ACKNOWLEDGMENTS

The authors thank Dr. Daniel K. Sodickson for his enthusiastic support and interesting discussions.

## REFERENCES

1. Hennig J, Naureth A, Friedburg H. RARE imaging: a fast imaging method for clinical MR. *Magn Reson Med* 1986;3:823–833.
2. Ordidge P, Howesman A, Coxon R, Chapman B, Turner R, Stehling M, Mansfield P. Snapshot head imaging at 0.5t using the echo planar techniques. *Magn Reson Med* 1988;8:110–116.
3. Hutchinson M, Raff U. Fast MRI data acquisition using multiple detectors. *Magn Reson Med* 1988;6:87–91.
4. Kwiat D, Einav S, Navon G. A decoupled coil detector array for fast image acquisition in magnetic resonance imaging. *Med Phys* 1991;18:251–265.
5. Ra JB, Rim CY. Fast imaging using subencoding data sets from multiple detectors. *Magn Reson Med* 1993;30:142–145.
6. Sodickson DK, Manning WJ. Simultaneous acquisition of spatial harmonics (SMASH): fast imaging with radiofrequency coil arrays. *Magn Reson Med* 1997;38:591–603.
7. Pruessmann KP, Weiger M, Scheidegger MB, Boesiger P. Sense: sensitivity encoding for fast MRI. *Magn Reson Med* 1999;42:952–962.
8. Pruessmann KP, Weiger M, Boernert P, Boesiger P. Spiral sense: sensitivity encoding with arbitrary  $k$ -space trajectories. In: *ISMRM Conference Abstracts*, 1999. p 94.
9. Hingham NJ. Accuracy and stability of numerical algorithms. Philadelphia: SIAM, 1996.
10. Brey WW, Narayana PA. Correction for intensity falloff in surface coil magnetic resonance imaging. *Med Phys* 1987;15:241–245.
11. Murakami JW, Hayes CE, Weinberger E. Intensity correction of phased-array surface coil images. *Magn Reson Med* 1996;35:585–590.
12. Pruessmann KP, Weiger M, Scheidegger MB, Boesiger P. Coil sensitivity maps for sensitivity encoding and intensity correction. In: *Proceedings of the ISMRM 6th Annual Meeting*, Sydney, 1998. p 2087.
13. Van Vaals JJ, Brummer ME, Dixon WT, Tuithof HH, Engels H, Nelson RC, Gerety BM, Chezmar JL, Den Boer JA. "Keyhole" method for accelerating imaging of contrast agent uptake. *J Magn Reson Imaging* 1993;3:671–675.

**Publication:**

Paper IV:

Line Scan Echo Planar Spectroscopic Imaging.

Authors:

Koichi Oshio, **Walid E. Kyriakos**, and Robert V. Mulkern.

Journal:

Magnetic Resonance in Medicine (MRM)

44: 521 – 524, 2000.

# Line Scan Echo Planar Spectroscopic Imaging

Koichi Oshio,<sup>1</sup> Walid Kyriakos,<sup>2</sup> and Robert V. Mulkern<sup>1,2\*</sup>

A line scan echo planar spectroscopic imaging (LSEPSI) sequence is presented which can rapidly produce 2D chemical shift imaging (CSI) data with minimal relaxation weighting and motion-related artifacts. The technique is based on successive "snapshot" 1D CSI acquisitions of individual tissue columns, and avoids  $T_1$  saturation problems associated with the short TR periods needed for very rapid scanning with either conventional or echo planar-based 2D CSI methods. Potential applications include rapid fat/water spectral quantitation in the abdomen and internally referenced temperature monitoring for interventional procedures. *Magn Reson Med* 44:521–524, 2000. © 2000 Wiley-Liss, Inc.

**Key words:** fast spectroscopic imaging; line scan; echo planar; chemical shift imaging; fat; water

Echo planar imaging (EPI) gradients enable signal readouts which simultaneously encode one spatial dimension and the spectral dimension (1–7). Combined with standard slice selection and phase encoding, scan times for 2D chemical shift imaging (CSI) experiments can be dramatically reduced compared to conventional CSI. In potential applications, such as in vivo tissue temperature monitoring for thermal therapy (8–10) or breath-hold fat/water spectral acquisitions in the body (11), it is desirable to decrease the 2D CSI scan times as much as possible. One obvious approach is to lower the TR of echo planar-based 2D CSI sequences to the limits dictated by the required spectral resolution. This invariably introduces  $T_1$ -related signal losses, which can be quite substantial for typical tissue  $T_1$  values (on the order of 1 sec). In this study, we generated 2D CSI data sets by combining line scan imaging methods with echo planar spectral/spatial readouts. The line scan imaging approach has previously been demonstrated in the context of spin density imaging (12),  $T_2$  measurement (13), and diffusion imaging (14). In the context of rapid spectroscopic imaging, the approach offers spectral data largely free from  $T_1$  relaxation loss, with minimal  $T_2$ -weighting. Furthermore, the lack of any phase encoding and the "snapshot" sampling of individual columns both help minimize motion ghosting artifacts. We demonstrate how the combination of all these features results in good signal-to-noise spectra for fat/water quantitation from 4096, 0.22 ml voxels in approximately 4 sec in the abdomen of a healthy volunteer.

## MATERIALS AND METHODS

The line scan echo planar spectroscopic imaging (LSEPSI) sequence shown in Fig. 1 was implemented on a 1.5 T LX scanner at the 8.2.5 hardware/software configuration (General Electric Medical Systems, Milwaukee, WI). The 90° and 180° pulses selected mutually orthogonal, 10-mm-thick slices inclined by 45° from the normal of the slice to be sampled. Rapid, successive column sampling was achieved by varying the RF pulse frequencies. The second half of the spin echo formed at TE = 10 msec from each column was sampled with an asymmetric echo planar gradient waveform (15) to simultaneously encode the along-column spatial dimension and the spectral dimension (6). We used 32 gradient echoes spaced by 1.3 msec, for a spectral resolution of 24 Hz. A receiver bandwidth of  $\pm 64$  kHz with 64 frequency encoding steps per gradient echo were employed for the along-column spatial sampling. A total of 64 columns were sequentially sampled at 62 msec intervals to cover the second in-plane dimension for a final 40 × 40 cm FOV in a 4 sec total scan time. Voxel dimensions were approximately 6 × 6 × 6 mm<sup>3</sup>. The slice thicknesses of the columns were chosen to fill the FOV while avoiding overlap between adjacent columns. In addition, sampling of the even and odd columns was staggered so as to further avoid potential saturation at column edges. The spoiler gradients following each echo planar acquisition were applied along varying spatial axes in a six-step phase cycling scheme (x, y, z, -x, -y, -z) to eliminate ghosting artifacts from indirect echoes (14). Individual column reconstructions in the form of 1D CSIs were performed using 2D Fourier transform along the spectral and along-column spatial dimension, with the final results displayed in magnitude mode. The along-column spatial and spectral dimensions were zero-filled to 128 from 64 and 32 samplings, respectively, prior to the Fourier transform.

## RESULTS

Figure 2a–c shows projection images generated from the 64 columns sampled with the 4 sec LSEPSI acquisition through the abdomen of a healthy 33-year-old male volunteer during a breath-hold. Figure 2a contains the signals from both the fat and water resonances, while Fig. 2b and c are images generated solely from the lipid resonances below 3.0 ppm and solely from the resonances above 3.0 ppm—showing primarily water, but also olefinic protons. The sampled columns are vertically oriented in these images, with the frequency readout direction being anterior to posterior. The liver and spleen are both seen in the water image; the spleen appears brighter due to a longer  $T_2$  than the liver. Abdominal fat is seen at a number of locations in the fat image (center). Three representative 1D CSIs of the 64 sampled (at columns 15, 45, and 55, respectively, along the x-axis of Fig. 2a–c at locations marked

<sup>1</sup>Department of Radiology, Brigham and Women's Hospital, Boston, Massachusetts.

<sup>2</sup>Department of Radiology, Children's Hospital, Harvard Medical School, Boston, Massachusetts.

A preliminary account of this work was presented at the 8th Annual Meeting of the ISMRM, Denver, CO, 2000 (Abstract 1832).

\*Correspondence to: Robert V. Mulkern, Department of Radiology, Children's Hospital, 300 Longwood Avenue, Boston, MA 02115. E-mail: mulkern@bwn.harvard.edu

Received 4 January 2000; revised 30 May 2000; accepted 21 June 2000.

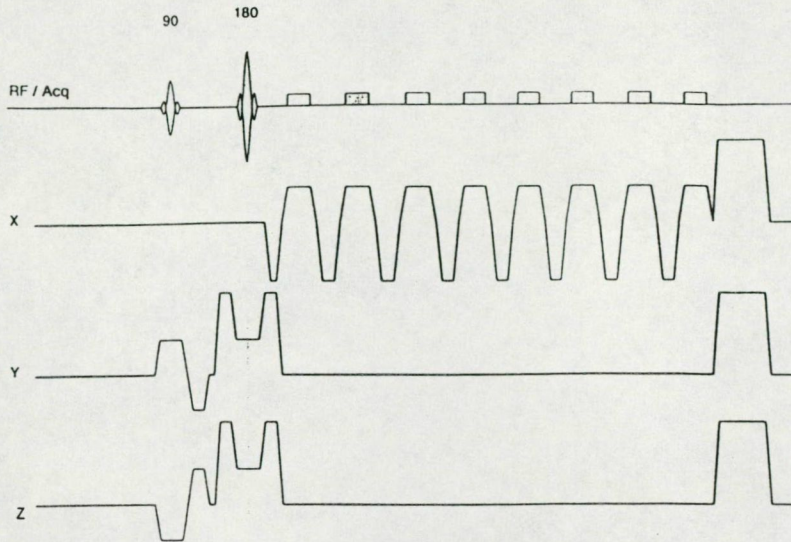


FIG. 1. LSEPSI sequence in which only eight gradient echoes of the 32 actually collected are shown.

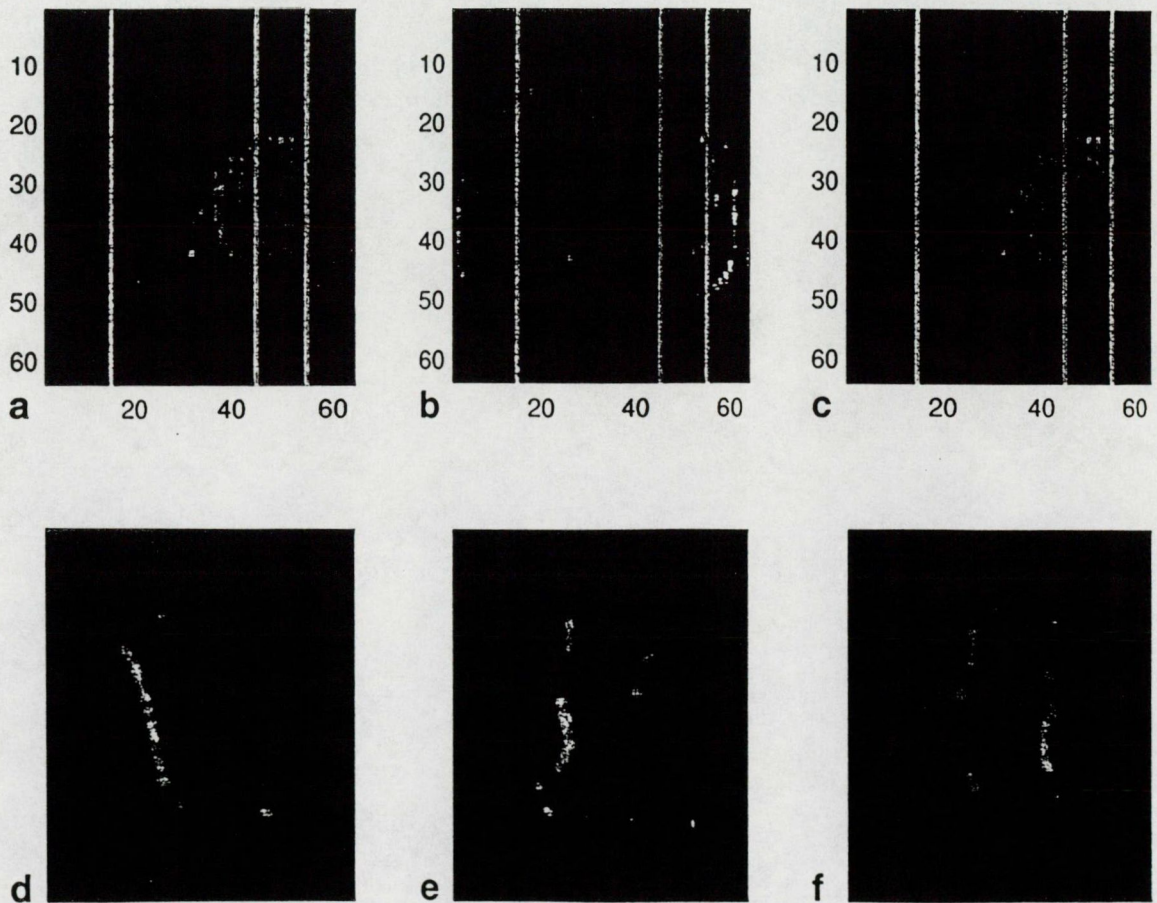


FIG. 2. **a:** Projection image made by summing the data from all 64 columns and all frequency bins. **b:** Projection image made by summing all 64 columns and frequency bins below 3.0 ppm showing primarily fat. **c:** Projection image made by summing all 64 columns and frequency bins above 3.0 ppm, showing primarily water with some olefinic signal at 5.4 ppm. **d:** 1D CSI from column 15, which passes from the posterior to anterior at a left-right location passing through the liver. The water resonance is to the left and the methylene resonance to the right in all 1D CSIs shown. The vertical axis is spatial with bottom-to-top corresponding to posterior-to-anterior anatomically. **e:** 1D CSI from column 45, passing primarily through the spleen. **f:** 1D CSI of column 55, passing through substantial deposits of abdominal fat as well as muscle in the anterior and posterior locations.

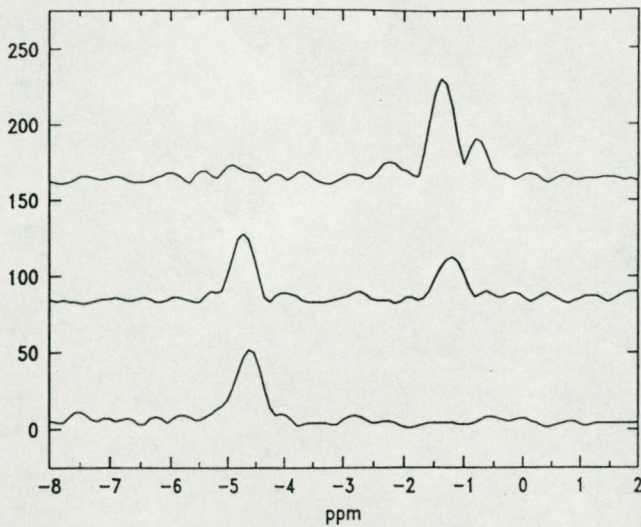


FIG. 3. Three representative spectra taken from the abdominal data acquired for Fig. 2. The lower spectrum is primarily a water signal in the liver, the middle spectrum is from a region containing some tissue and abdominal fat, and the top spectrum is from a region largely containing only abdominal fat.

with white vertical lines) are shown in Fig. 2d–f. In each 1D CSI the water band is to the left, as in conventional spectroscopic formats. The vertical axis, taken from bottom to top, corresponds to posterior-to-anterior anatomy. The 1D CSI shown in Fig. 2d, column 15, passes through the liver and contains mostly water signal, except at the edges of the body where the subcutaneous lipid signal is seen. The 1D CSI shown in Fig. 2e contains mostly water signal from the spleen, with subcutaneous fat at the edges of the body. The 1D CSI shown in Fig. 2f contains substantial portions of abdominal fat as well as muscle in the posterior and anterior locations. The curvature of the water resonance with position along the columns is due to field variations along the columns.

Figure 3 provides representative spectra extracted from

two locations in column 55 and one in column 15. The spectra have been chosen from locations which progressively demonstrate water to lipid rich regions (bottom to top, respectively), sampling pure liver, an abdominal fat/tissue and water region, and a pure abdominal fat region. The signal-to-noise ratio (SNR) for the single water resonance in the liver (lower spectrum) is approximately 14, while the SNR for the methylene resonance in the primarily abdominal fat spectrum (top) is approximately 18, as estimated from peak heights over baseline noise values in these magnitude spectra.

Figure 4a and b shows 1D CSIs from a corn oil phantom floating within tap water. The  $T_1$ s of the tap water and corn oil were estimated to be approximately 5 sec and 0.5 sec, respectively, using signal intensity measurements from fast spin echo (FSE) images acquired with four different TR values. The images in Fig. 4 are windowed to provide similar visual signal intensities from the corn oil signal in the center of the phantom. The 1D CSI of Fig. 4a arises from an echo planar spectroscopic sampling acquisition of a single column repeatedly scanned with a TR of 500 msec. A total of 16 signal averages were used along with 8 dummy acquisitions preceding the 16 single-shot data collections. Note how the water resonances at the top and bottom of the phantom are smaller in signal intensity than the corn oil methylene resonance due to a  $T_1$  saturation effect, as would occur in conventional or echo planar-based 2D CSI methods with a 500 msec TR period. Figure 4b shows a 1D CSI from an LSEPSI acquisition using parameters identical to those employed for the abdominal imaging of Fig. 2. Strong water signals are now observed due to the infinite TR despite the 4 sec acquisition for all 64 columns. The water/methylene peak height ratio in Fig. 4a was 0.6, compared to a value of 2.2 for the infinite TR case of Fig. 4b, clearly demonstrating the TR saturation effect on the water resonance in the former.

## DISCUSSION

With phase-encoded 2D CSI methods, conventional or EPI based, TR values of 100 msec or less will result in signal

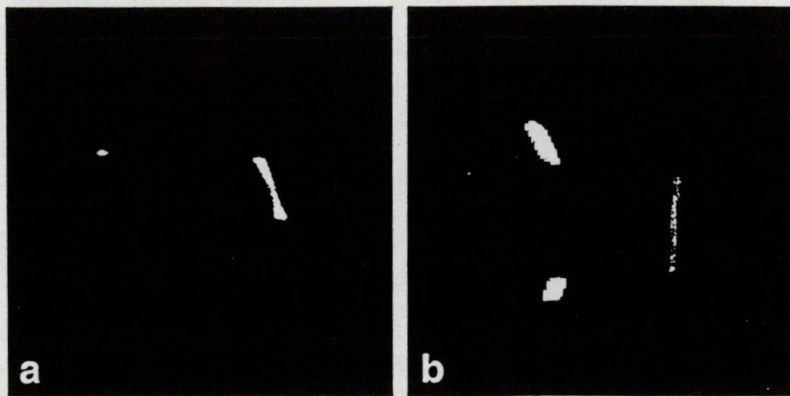


FIG. 4. a: 1D CSI through a water/corn oil phantom collected using 8 dummy scans and 16 signal averages with a 500 msec TR. Note that the water lines at the top and bottom of the column are less intense than the methylene resonance from the corn oil. b: 1D CSI taken from a 4 sec LSEPSI acquisition which sampled 64 columns of the water/corn oil phantom with an effective TR of infinity. Note that now the signal intensity, from the water resonances are larger than the corn oil methylene resonance since there is no  $T_1$  saturation of the water lines, as occurs during repeated sampling of the column at 500 msec intervals (a). a and b were generated from scans on different days, so while the columns shown are not identical they share the same basic geometry with respect to the oil vial and water bath.

losses of 80 to 90% from tissues with  $T_1$  values of 1 sec even when optimized flip angles are employed. Using the line scan approach, this  $T_1$ -related signal is largely restored even though the individual columns are sampled at "TR" intervals less than 100 msec. From the  $T_1$  relaxation point of view, the TR is effectively infinite for single excitation line scanning. There is, of course, an inherent signal loss when 1D column sampling is compared with 2D planar sampling. For equivalent voxel dimensions this loss is equal to the square root of the number of phase encodes. For the example we have used, in which 64 columns instead of 64 phase encodes were sampled, a factor of 8 reduction in signal-to-noise (S/N) is to be expected with line scan vs. 2D planar sampling. This fundamental reduction in S/N must be weighed against the potentially useful  $T_1$ -related signal gains achieved with line scanning when comparing the method with phase-encoded echo planar spectroscopic imaging for any given application. For instance, mapping low concentration metabolite signals in the brain generally utilizes long TR values for various reasons, including long signal readouts and water and outer volume suppression pulse modules (4,5,16). Under such circumstances, line scanning with multiple signal averaging offers no obvious advantages over phase-encoded echo planar spectroscopic imaging. In situations where the combination of rapid acquisitions and minimal relaxation losses are desired for spectral quantitation of major resonances like fat and water, however, the line scan approach may be quite attractive. We have attempted to demonstrate this capability with a 4 sec breath-hold abdominal study. In applications where rapid acquisitions are desired, and limited volume coverage and spatial resolution suffice, the line scan method generally will be advantageous over alternative planar phase-encoding strategies. This is because the use of a small number of phase-encoding steps invariably leads to substantial signal bleed along the phase-encode dimension (17), whereas reducing the number of columns sampled with line scanning methods does not degrade the spatial mapping of the volume covered. Finally, motion ghosting artifacts will be minimized with line scan acquisitions because of the lack of any phase encoding, and because the "snapshot" nature of the individual column sampling can freeze motion-related problems to a large extent. In 2D echo planar spectroscopic imaging with phase encoding, motion at any time throughout the full scan cycle from any structure within the FOV will degrade the entire spectroscopic image data set.

In conclusion, there are several features of LSEPSI which may be of value for certain applications. The precise column thicknesses, number of gradient echoes, spectral bandwidths, number of columns sampled, and number of frequency-encoding steps must be carefully considered for each application so that appropriate combinations of signal-to-noise, spatial, spectral, and temporal resolutions are found. One application in which the technique should prove useful is in rapid fat/water spectral quantitation in

the abdomen (11), or possibly even the heart, where motion artifacts can be quite severe. Another potential application is for internally referenced temperature monitoring during thermal therapy (8–10). Rapid mapping of fat/water frequency differences in the breast with LSEPSI may ultimately provide robust, motion insensitive, internally referenced (8) temperature monitoring for precise thermal therapy.

## ACKNOWLEDGMENTS

We thank Lawrence Panych, Ph.D., for helpful discussions during the course of this work.

## REFERENCES

- Mansfield P. Spatial mapping of the chemical shift in NMR. *Magn Reson Med* 1984;1:370–386.
- Matsui S, Sekihara K, Kohno H. High speed spatially resolved NMR spectroscopy using phase-modulated spin-echo trains. Expansion of the spectral bandwidth by combined use of delayed spin-echo trains. *J Magn Reson* 1985;64:167–171.
- Webb P, Spielman D, Macovski A. A fast spectroscopic imaging method using a blipped phase encode gradient. *Magn Reson Med* 1989;12:306–315.
- Posse S, DeCarli C, Le Bihan D. 3D echo-planar MR spectroscopic imaging at short echo times in human brain. *Radiology* 1994;192:733–738.
- Posse S, Gioacchino T, Risinger R, Ogg R, Le Bihan D. High speed 1 H spectroscopic imaging in human brain by echo-planar spatial-spectral encoding. *Magn Reson Med* 1995;33:34–40.
- Bao S, Guttman CRG, Mugler III JP, Brookeman JR, Panych LP, Kraft RA, Oshio K, Jaramillo D, Jolesz FA, Williamson DS, Mulkern RV. Spin-echo planar spectroscopic imaging for fast lipid characterization in bone marrow. *Magn Reson Imaging* 1999;17:1203–1210.
- Pohmann R, von Kienlin M, Haase A. Theoretical evaluation of fast chemical shift imaging methods. *J Magn Res* 1997;129:145–160.
- Kuroda K, Oshio K, Mulkern RV, Panych LP, Okuda S, Hynynen K, Jolesz FA. Temperature mapping using the water proton chemical shift: self-referenced method with echo planar spectroscopic imaging. *Magn Reson Med* 2000;43:220–225.
- Mulkern RV, Panych LP, McDannold NJ, Jolesz FA, Hynynen K. Tissue temperature monitoring with multiple gradient echo imaging sequences. *J Magn Reson Imaging* 1998;8:493–502.
- Mulkern RV, Chung A, Jolesz FA, Hynynen K. Temperature monitoring of ultrasonically heated muscle with RARE chemical shift imaging. *Med Phys* 1997;24:1899–1906.
- Shinmoto H, Oshio K, Jolesz FA, Mulkern RV. A breath-hold chemical shift imaging approach for fatty liver assessment. In: *Proceedings of the 4th Annual Meeting of ISMRM*. New York, 1996. p 1049.
- Maudsley AA. Multiple line-scanning spin density imaging. *J Magn Reson* 1980;41:112–126.
- Shioya S, Christman R, Ailion DC. An in vivo NMR imaging determination of multiexponential Hahn T2 of normal lung. *Magn Reson Med* 1990;16:49–56.
- Gudbjartsson H, Maier SE, Mulkern RV, Morocz IA, Patz S, Jolesz FA. Line scan diffusion imaging. *Magn Reson Med* 1996;36:509–518.
- Feinberg DA, Turner R, Jakab PD, von Kienlin M. Echo-planar imaging with asymmetric gradient modulation and inner-volume excitation. *Magn Reson Med* 1990;13:162–169.
- Gonen O, Arias-Mendoza F, Goelman G. 3D localized in vivo  $^1\text{H}$  spectroscopy of human brain using a hybrid of 1D-Hadamard with 2D-chemical shift imaging. *Magn Reson Med* 1997;37:644–650.
- Maudsley AA, Matson GB, Hugg JW, Weiner WM. Reduced phase encoding in spectroscopic imaging. *Magn Reson Med* 1994;31:645–651.